# Contributions to Precision and Accuracy of Chemical Ages of Monazite

**Joseph M. Pyle*[,1], Frank S. Spear[1], David A. Wark[1], Christopher G. Daniel[2], and Lara C. Storm[1]**

1: Department of Earth and Environmental Sciences, Rensselaer Polytechnic Institute, Troy, NY, USA, 12180-3590

2: Department of Geology, Bucknell University, Lewisburg, PA, USA, 17837

*Email: pylej@rpi.edu

**Abstract**

Systematic analysis of monazite is undertaken to determine the factors controlling the precision and accuracy of chemical monazite dating by electron microprobe (EMP). For this study, a JEOL 733 Superprobe EMP, equipped with 4 PET diffraction crystals, and both argon and xenon detectors, is employed. Besides U, Th, and Pb, Y is analyzed for calculation of interference correction factors, and Ce is analyzed as a monazite monitor element. U Mβ is selected for analysis over U Mα due to the lesser interference of Th Mγ vs. Th Mβ, and the proximity of U Mα to the Ar K absorption edge. Optimization of lead analysis precision, which is the limiting factor in age precision, is achieved in the following manner. Pb Mα is chosen for analysis over Pb Mβ, as the analytical precision for Pb Mα, after correction for Th and Y interference, is, with the exception of very (> 10-15 wt. %) Th-rich samples, greater than the analytical precision associated with analysis of Pb Mβ. Xe detectors are favored over Ar detectors for Pb analysis, as: 1) Xe background is flatter than Ar background in the region of Pb Mα peak and background, enabling two-point background collection and linear interpolation; 2) the use of Ar detector gas generates non-filterable second order LREE escape peaks. The second order Ce Lα escape peak interferes with Pb Mβ, increasing the apparent lead concentration in an average monazite (25-28 wt% Ce) by 200-250 ppm, inducing a minimum systematic inaccuracy of 25-33 % for mid-Paleozoic monazites of typical metamorphic composition (2000-6000 ppm U, 3-5 wt. % Th). For EMPs with adjustable X-ray collimators, the combination of high peak intensity and high peak-to-background is maximized for measurement of Pb Mα on a Xe detector with the collimator at maximum width setting. Using the above settings and peak selections, analytical precisions of

the following levels are obtainable for typical metamorphic monazites (1σ relative standard deviation): Th, 0.5-2.0%; U, 1.5-3.0%; Pb, 1-4 % for mid-Proterozoic monazites, and 3-18% for mid-Paleozoic (400-300 Ma) monazites, translating to 1σ age uncertainties of approximately 40-50 Ma for both monazite age groups above, with increased (i.e., smaller) precisions of *identifiably distinct* age, compositional, or reaction domains described by the standard error of the mean associated with the average age of the domain. Machine settings for EMP chemical age analysis of monazite include 25 keV accelerating voltage, 200 nA Faraday cup current for analysis and 10 nA for calibration. Variable current settings for calibration and analysis are adopted to minimize detector voltage pulse shift; PHA voltage window widths are set narrow to exclude higher-order peaks, but wide enough to minimize the potential of voltage pulse clipping, and concomitant decrease in apparent concentration. Variable background settings are also adopted for calibration and analysis. Pb Mα is analyzed simultaneously on two spectrometers, with a beam diameter of 5-7 mm, and 3 minutes of analysis each of lead peak and background positions per spot; a 6 minute, single-spot cycle can be repeated to improve single-spot precision, barring evidence of sample damage, such as carbon coat bubbling, absorbed current drop, large fluctuations in element concentration, or surface burn-through. Prior to analysis, correction factors for Th and Y interference on Pb Mα are measured, and the Pb standard k-ratio is measured before, during, and after analysis to monitor for spectrometer drift, and to correct for drift, if necessary. The accuracy of monazite chemical age analyses can not be rigorously quantified without synthetic monazite age standards, but semi-quantifiable contributors to systematic error include poorly characterized primary or secondary standards, pulse shift, dead time, spectrometer drift, and uncertainty in ZAF model corrections. Following the above procedures reduces systematic errors due to peak shift and pulse drift. Additional sources of systematic error include sample damage during analysis, and errors in ZAF or ϕρz corrections relating to monazite grain size, location, orientation and homogeneity. We suggest adoption of a maximum acceptable (U+Th+Pb) analytical precision of ±25% (1σ), which yields, for a single 6-minute analysis, a lead detection limit of 300-320 ppm, or an age limit of ~150 Ma for metamorphic monazites of average composition; lead precision increases and minimum age decreases by $\sqrt{n}$, where n is the number of 6-minute cycles measured on a single spot. Using this protocol, we reproduce, within error (1σ 10-40 Ma), $^{207}Pb/^{206}Pb$ ages of ~420 Ma for a monazite in aluminous schist from the Chester Dome, VT, USA.

## INTRODUCTION

The recognition by Parrish (1990) that monazite incorporates little to no common lead spurred investigators to attempt *in-situ* dating of monazite with the electron microprobe (EMP). Monazite is an ideal candidate for mineral dating; in addition to its propensity to exclude common lead, it also may incorporate significant amounts of Th and U (Spear and Pyle, 2002, and references therein), leading to accumulation of measurable amounts of radiogenic Pb within 50-150 Ma, depending on original Th and U concentration. Diffusion of Pb in monazite is virtually negligible (Cherniak et al., submitted); the lead closure temperature for a 10 μm grain cooling at 10°C/My is approximately 900°C. Monazite is also highly resistant to metamictization (Karioris et al., 1991; Meldrum et al., 1997), so lead loss via accumulated lattice damage is unlikely.

Suzuki and Adachi (1991) and Suzuki et al. (1994) pioneered EMP chemical dating of monazite. Statistical treatment of monazite chemical ages was addressed by Montel et al. (1996), using the methods of Wendt and Carl (1991), and Williams et al. (1999) produced the first monazite age maps by running background-subtracted U, Th, and Pb pixel values through the chemical age equation for monazite (e.g., Montel et al., 1996):

$$Pb = Th/232\left[e^{\lambda^{232}\tau} - 1\right]208 + (U/238{\cdot}04)0.9928\text{x}\left[e^{\lambda^{238}\tau} - 1\right]206 + (U/238{\cdot}04)0.0072\text{x}\left[e^{\lambda^{235}\tau} - 1\right]207 \quad (1)$$

The relative abundance of EMPs relative to in-situ isotopic analyzers has lead to a proliferation of published chemical monazite dates for both ancient and recent igneous, sedimentary, and metamorphic rocks (Kim et al, 1997; Pan and Stauffer, 2000; Cho et al., 1999; Grew et al., 2001; Asami et al., 2002; Boggs et al. 2002) as well as attempts to date

deformational episodes (Krohe and Wawrzenitz, 2000; Williams and Jercinovic, 2002; Bell and Welch, 2002) and metamorphic reactions (Foster et al., 2002; Catlos et al., 2002; Pyle and Spear, 2003).

However, EMP chemical dating of monazite is beset by a number of uncertainties and difficulties, making a rigorous assessment of the accuracy and precision associated with each chemical age a non-trivial task. Moreover, potential problems with the method are introduced at almost all junctures of the analytical process, including sample preparation, calibration, analysis, and post-analysis data reduction, as discussed by Scherrer et al. (2000).

For any monazite chemical analysis, the goal is to obtain the most precise and accurate analysis possible. Foremost in this process is the recognition that variation in monazite grain size, orientation, textural setting, and compositional/age zonation may preclude the development of a single monazite chemical dating protocol, and instead emphasize the need for analytical flexibility. In this light, we will discuss analytical precision, in the context of optimizing Pb analysis, along with other crucial elements (U, Th, Y, and Ce). A step-by-step analytical protocol is presented, highlighting the relationship between EMP settings and potential analytical artifacts that are detrimental to accurate chemical dating of monazite. Estimating accuracy of monazite analyses is addressed, and we discuss further requirements for, and advantages and limitations of, the chemical dating technique by comparison of chemical and isotopic age analyses. A complete worked example of monazite chemical age analysis from the Paleozoic of central New England, U.S.A., is presented in the appendix.

## EMP HARDWARE SPECIFICS

### EMP Models in use

Two manufacturers account for the overwhelming majority of EMPs in use both in industry and academia; JEOL (Tokyo, Japan), and CAMECA (Paris, France). Although the EMP platforms of each manufacturer are broadly similar, differences do exist between the current and older models of both companies. These differences are notable enough to affect the development of analytical protocols on different model EMPs.

A basic overview of JEOL and CAMECA EMPs is presented below. Other EMP models still in use include platforms manufactured by Thermo ARL, formerly ARL (Ecublens, Switzerland), and ETEC (no longer in operation). These platforms are not discussed further, but the protocols presented below are applicable to the extent that basic similarities exist between all wavelength dispersive EMPs.

### JEOL

The current JEOL EMP production model is the JEOL 8200; other models still in use include the JEOL 8900 and JEOL 733 Superprobe. The protocol presented in this paper was developed on a JEOL 733 Superprobe manufactured in 1985-1986.

Beam energies of 1-35 keV are accessible on JEOL EMPs, and beam currents of ~50 pA to 2.0 μA are obtainable, with a full range of adjustable beam diameters (1-50 μm). JEOL EMPs incorporate a 140 mm Rowland circle, with a sample X-ray take-off angle of 40°. All wavelength dispersive (WD) scans presented below are referenced to a 140 mm Rowland circle, and thus are not directly applicable to EMPs incorporating a 160 mm or 100 mm Rowland circle. Up to five WD spectrometers can be incorporated in JEOL EMPs, and each spectrometer in the RPI 733 Superprobe is equipped with two swappable diffraction crystals. Four of the five spectrometers

on the RPI 733 Superprobe are equipped with PET (pentaerythritol) diffraction crystals, enabling simultaneous detection of Pb X-rays on as many as three spectrometers, with concurrent detection of U and Th on the fourth PET-bearing spectrometer.

All JEOL models may incorporate either Argon- (P10) or Xenon-based X-ray detectors. The RPI 733 Superprobe incorporates Ar detectors with spectrometers 1-3 and Xe detectors with spectrometers 4 and 5.

JEOL EMPs also contain adjustable X-ray collimators. Adjustable X-ray collimators aid minimizing X-ray beam divergence and defocusing brought about by the Johann (1931) focusing arrangement for diffraction crystals, such as PET, that tend to degrade with surface grinding. Surficial grinding of the diffraction crystal is a necessary component of the Johannson (1933) focusing arrangement, but owing to crystal degradation in PET and LiF, Johannson focusing is not commonly adapted. The X-ray collimators in the RPI 733 Superprobe are adjustable to widths of 3 mm ("open setting"), 500 μm, and 300 μm.

**CAMECA**

CAMECA's current production model EMP is the SX-100, but older SX-50s and CAMEBAX models are still in use. The CAMECA SX-100 houses up to five WD spectrometers, and incorporates a 40° sample X-ray take-off angle, as do current and older JEOL models. The range of attainable beam energy and currents are similar to those of JEOL EMPs. However, three significant differences exist between CAMECA and JEOL EMPs. First, Rowland circle configurations on the SX-100 and older CAMECA EMPs are of the 160 mm variety. Second, CAMECA EMPs do not contain adjustable X-ray collimators. Third, all CAMECA EMP X-ray detectors use Ar (P10) detector gas; for higher-energy X-rays ($\lambda < 3$ Å), Ar gas pressure is increased to 2-3 atm to increase ionization efficiency.

The results of our study are applicable, in a general sense, to both CAMECA and JEOL EMPs. However, variations in platform configuration between JEOL and CAMECA should be noted. The difference in Rowland circle configurations means that background offsets are not platform portable. The discussion on X-ray collimation is not valid for CAMECA EMPs. Finally, the lack of Xe detectors on CAMECA EMPs provides an additional (but not insurmountable) obstacle to obtaining precise and accurate chemical monazite ages; the basis of this argon-related issue is explained below.

## PRECISION IN CHEMICAL DATING OF MONAZITE

### Poisson Statistics

For the purposes of discussion, it is assumed that the precision of a chemical age estimate of monazite is solely a function of the counting (Poisson) statistics of the elemental concentrations measured during analysis. Systematic errors arising from EMP configuration, data reduction, inherent monazite properties, or some combination thereof, are addressed in the section on analytical accuracy.

The basics of Poisson statistics, as applied to EMP analysis, are presented by Scott et al. (1995), and summarized briefly here. Precision in Poisson statistics is a function of the accumulated number of counts, with the standard deviation of accumulated counts $N$ given by $\sigma_N = \sqrt{N}$, and with a relative standard deviation (fraction or percent) of $\frac{\sqrt{N}}{N}$, or $\frac{1}{\sqrt{N}}$. As accumulated counts of the unknown are referenced to accumulated standard counts, from both peak and background positions, acquired during calibration, the precision of the unknown k-ratio is a function of both peak counts (P) and background counts (B) on the unknown and standard.

The standard deviation $\sigma_{P\text{-}B}$, and relative standard deviation $\varepsilon_{P\text{-}B}$ for both the standard and unknown, in units of counts per unit current-time (cts/nA•sec) is calculated as

$$\sigma_{P-B} = \sqrt{\left(\frac{N_P}{t_P^2 curr_P^2}\right) + \left(\frac{N_B}{t_B^2 curr_B^2}\right)} \tag{2a}$$

$$\varepsilon_{P-B} = \sqrt{\left(\frac{N_P}{t_P^2 curr_P^2}\right) + \left(\frac{N_B}{t_B^2 curr_P^2}\right)} \Bigg/ \left[\left(\frac{N_P}{t_P curr_P}\right) - \left(\frac{N_B}{t_B curr_B}\right)\right] \tag{2b}$$

The standard deviation of the k-ratio ($\sigma_{P\text{-}B,k\text{-}ratio}$) is found by applying the simplified formula (all covariance terms equal to zero) for the standard deviation of a ratio *a/b* (Bevington, 1969); *a*, in this case, is the formula for the standard deviation of P-B counts on the unknown, and *b* is the formula for the standard deviation of the P-B counts on the standard. Partial differentiation of *a* and *b* with respect to *a/b* yields

$$\sigma_{P-B,k-ratio}^2 = \left( \frac{1}{2\left(\frac{N_{P,unk}}{t_{P,unk}^2 curr_{P,unk}^2} + \frac{N_{B,unk}}{t_{B,unk}^2 curr_{B,unk}^2}\right)^{1/2} \left(\frac{N_{P,std}}{t_{P,std}^2 curr_{P,std}^2} + \frac{N_{B,std}}{t_{B,std}^2 curr_{B,std}^2}\right)^{1/2}} \right)^2 \sigma_{P-B,unk}^2 + \left( -\frac{1}{2} \bullet \frac{\left(\frac{N_{P,unk}}{t_{P,unk}^2 curr_{P,unk}^2} + \frac{N_{B,unk}}{t_{B,unk}^2 curr_{B,unk}^2}\right)^{1/2}}{\left(\frac{N_{P,std}}{t_{P,std}^2 curr_{P,std}^2} + \frac{N_{B,std}}{t_{B,std}^2 curr_{B,std}^2}\right)^{3/2}} \right)^2 \sigma_{P-B,std}^2 \tag{3a}$$

The relative standard deviation of peak minus background counts on the k-ratio is given by

$$\varepsilon_{P-B,k-ratio} = \sqrt{\varepsilon_{P-B,std}^2 + \varepsilon_{P-B,unk}^2} \tag{3b}$$

The calculation of the statistic in equation (3a) is simpler, and the relative standard deviation is a more useful value, as it relates directly to the uncertainty in the age calculation for a single

analysis. Assuming that X-ray production scales linearly with current, count accumulation to the desired precision may be achieved by maintaining a constant current-time (nA•sec) product.

With the exception of Proterozoic or older, U-poor monazites (e.g., Daniel and Pyle, 2002), the limiting factor in monazite chemical age analysis is the precision associated with Pb analysis. Thus, optimization of lead analysis for maximum precision will, in most cases, result in the most precise chemical age determination. However, the precision associated with the analyses of other elements, as well, has a direct bearing on the final precision of the Pb analysis.

**Element Selection**

At a minimum, three elements must be analyzed simultaneously to obtain monazite chemical ages (eqn. 1); Th, U, and Pb. Depending on the Pb line (Mα or Mβ) chosen for analysis, Y and/or Ce must be analyzed to provide information for interference corrections. The concentrations of all common monazite elements (REE, Ca, Si, P) are fixed to provide a matrix for ZAF or φρz corrections. Pyle (2001) presented an average of 529 monazite analyses used in ZAF corrections for chemical monazite ages (Table 1).

Software packages such as Virtual WDS (Reed and Buckley, 1996) generate "virtual" monazite spectra (Fig.1) that are much easier to interpret than the complex WD spectra of natural monazite (Pyle et al., 2002), thus aiding in element interference identification and X-ray line selection. For the Siegbahn notations used in this paper, absence of a subscript implies that the line under discussion is a resolvable "1" line, e.g. U Mα is equivalent to U $M\alpha_1$. For typical monazite compositions, the Lα lines of Ce and Y are free from interference, as is the Mα line of Th. Both uranium M lines are subject to interference; Th Mβ interferes with U Mα (Fig. 1a) and Th Mγ interferes with U Mβ (Fig 1b). Lead Mα and Mβ are subject to interference as well; Pb

Mα by first-order Th $M\zeta_{1,2}$, second-order Th M2-O4 and first-order Y $L\gamma_{2,3}$ (Fig 1c), and Pb Mβ by U Mζ (first order) and potentially by S Kβ (first order and Ce Lα (second order).

Analysis of U Mβ is favored for two reasons. First, the correction for Th Mγ interference is approximately one-half the correction for Th Mβ interference (Pyle et al., 2002), so errors associated with the interference corrections are reduced accordingly. Second, as noted by Suzuki and Adachi (1991), the proximity of U Mα to the Ar K absorption edge complicates background placement for U Mα analysis with Ar detectors. WD scans of monazite in the region of the Ar K absorption edge (Fig. 2) demonstrate that U Mβ provides a cleaner analysis, but that background placement in the vicinity of the Ar K absorption edge is crucial for U Mβ analysis as well. The correct low background placement is at position "a" (Fig. 2), and Table 2 shows the range in calculated ages (for fixed Th and Pb) associated with selection of low background positions "b" and "c".

**Special considerations for selection of lead analytical line**

Lead concentration in Paleozoic monazite is commonly an order of magnitude lower than that of uranium, and may be over two orders of magnitude lower than thorium concentration. As a result, determination of whether Pb Mα or Pb Mα yields the more precise analysis is non-trivial, and is further a multi-variable function of the inherently low Pb concentration of Paleozoic monazite, element interferences for both the Pb Mα and Mβ lines (Fig 2c,d), and EMP analytical considerations unique to lead. To determine the lead line that yields a more precise analysis, we consider: 1) relative intensities of the Pb Mα and Pb Mβ lines; 2) Pb analytical interferences, their correction, and error propagation associated with interference-corrected lead analysis; 3) detector gas, the formation of escape peaks, and escape peak interference with lead analysis; 4) the effect of variable X-ray collimator setting on monazite WD spectra, and; 5)

modeling of background radiation curvature and positioning of background collection during lead analysis.

***Pb line intensity*** The β/α intensity ratio for M line X-rays is generally given as 0.6 (Goldstein et al., 1984). However, for both M lines and L lines, the β/α intensity ratio is a function of atomic number, and varies significantly across an element group such as the actinides or the REE (Goldstein et al., 1984; Roeder, 1985). $PbSiO_3$ measured on the RPI 733 Superprobe (Fig. 3) yields a peak minus background Pb Mα/Pb Mβ intensity ratio of ~0.8.

***Pb elemental interferences, correction, and associated error propagation*** Figures 2c and 2d indicate that both Pb Mα and Mβ are affected by elemental interference. X-ray lines interfering with Pb Mα include Y $L\gamma_{2,3}$, first-order Th $M\zeta_1$ + Th $M\zeta_2$, and second-order Th M2-O4 (Fig. 2c). Second-order La Lα may interfere with Pb Mα if Ar detector gas is used (see below). First-order U $M\zeta_2$ interferes with Pb Mβ (but negligibly for monazites under 2 wt. % U), as does first order S Kβ, in S-rich monazites containing 0.1-0.5 wt. % S (Pyle and Spear, unpublished data). Second-order Ce Lα does not appear to interfere with Pb Mβ (Fig. 2d), but does if Ar detector gas is used (see below).

Considering solely peak intensity, Pb Mα yields a more precise analysis than Pb Mβ. However, the interferences on both lead peaks decrease Pb analytical precision, as the corrected Pb concentration is a function of the interfering elements, each of which carries analytical uncertainty. To determine whether a corrected Pb Mα analysis (with Th and Y interference) is less precise than a corrected Pb Mβ analysis (with U interference), the analytical uncertainties in the measured and interfering elements must be propagated through the equation for interference-

corrected concentration. Standard error propagation techniques are given in Bevington (1969), and in this case, all covariance terms are assumed to be zero.

Correction for interference of element *x* on element *y* requires measurement of the apparent concentration of element *y* in the y-free standard for element *x*. The correction factor for the interference of *x* on *y* ($CF_{x\text{-}y}$) is calculated as:

$$CF_{x-y} = y_{k-ratio}^{std,x} / x_{k-ratio}^{std,x} \sim y_{k-ratio}^{std,x} \tag{4}$$

and the corrected concentration in the unknown is calculated as:

$$y_{corr(wt\%)}^{unk} = y_{uncorr(wt\%)}^{unk} - \left(CF_{x-y}\right)\left(x_{k-ratio}^{unk}\right) \tag{5a}$$

or, alternately

$$y_{corr(k-ratio)}^{unk} = y_{uncorr(k-ratio)}^{unk} - \left(CF_{x-y}\right)\left(x_{k-ratio}^{unk}\right) \tag{5b}$$

The difference in application of equation (3a) vs. (3b) to correct for interference is negligible, as long as k-ratios, and not concentrations, are used in for both the correction factor and the interfering element in the unknown. Application of (5a) requires application of a ZAF correction after the interference correction is made, whereas (5b) does not. In the case of Pb Mα, an equation of the form of (5a) or (5b) is used, and the correction factor is summed over the interference contributions from Th (M$\zeta_{1,2}$ + M2-O4) and Y L$\gamma_{2,3}$, namely:

$$Pb_{corr(wt\%)}^{unk} = Pb_{uncorr(wt\%)}^{unk} - \left[\left(CF_{Th-Pb}\right)\left(Th_{k-ratio}^{unk}\right) + \left(CF_{Y-Pb}\right)\left(Y_{k-ratio}^{unk}\right)\right] \tag{6}$$

An equivalent equation can be written with the Pb k-ratio of the unknown.

As a result of this correction, the precision of the lead analysis decreases, because: 1) some portion of the measured counts at the Pb peak position are generated from Th M2-O4 and $M\zeta_{1,2}$ plus Y $L\gamma_{2,3}$ X-rays, and; 2) the corrected concentration of Pb is a function of the uncorrected concentrations of Pb, plus the measured concentrations of Y and Th in the unknown, along with the correction factors for interference of these elements, each of which carries an inherent statistical uncertainty.

The corrected analytical precision of lead is calculated as follows. First, the measured number of Pb counts in the unknown must be corrected for interference by Th + Y:

$$\text{Counts } Pb_{unk}\text{, corrected} = \text{counts } Pb_{unk}\text{, uncorrected} - (\text{counts } Th_{unk} * (CF_{Th\text{-}Pb}) + \text{counts } Y_{unk} * (CF_{Y\text{-}Pb})) \quad (7)$$

with the correction factors $CF_{x\text{-}y}$ as defined in equation (2) of the text. In some cases, the corrected lead counts may be 5-8% less than measured lead counts.

After Pb peak counts are corrected, the new statistical uncertainties, based on corrected U and Pb counts, are calculated. The simplified formula for error propagation for a = f(x,y), assuming all covariance terms equal zero, is:

$$\sigma_a^2 = \sigma_x^2\left(\frac{\partial a}{\partial x}\right)^2 + \sigma_y^2\left(\frac{\partial a}{\partial y}\right)^2 \quad (8)$$

Corrected Pb is a function of uncorrected Pb, plus Th and Y, according to (7) and (4), as:

$$Pb_{corr,unk} = Pb_{uncorr,unk} - \left[ \left( \frac{\frac{Pb_{Th\,std}}{Pb_{Pb\,std}}}{\frac{Th_{Th\,std}}{Th_{Th^o std}}} \right) \bullet Th_{unk} + \left( \frac{\frac{Pb_{Y\,std}}{Pb_{Pb\,std}}}{\frac{Y_{Y\,std}}{Y_{Y^o\,std}}} \right) \bullet Y_{unk} \right] \tag{9}$$

Each term represents the measured intensity (counts/nA•sec) of the indicated element in the indicated standard. The superscript "o" indicates a calibration-current measurement of 10 nA on the standard; all other measurements are taken at an analysis-current measurement of 200 nA, regardless of whether the material is a standard, or an unknown.

Expanding equation (8) about equation (9) yields 10 partial derivatives, with the dependent variable $Pb_{corr,unk}$ a function of the 10 independent variables $Pb_{uncorr,unk}$, $Pb_{Th\,std}$, $Pb_{Pb\,std}$, $Th_{Th\,std}$, $Th_{Th^o std}$, $Th_{unk}$, $Pb_{Y std}$, $Y_{Y std}$, $Y_{Y^o std}$, and $Y_{unk}$, each with associated uncertainty $\sigma_{Pb,uncorr,unk}$, $\sigma_{PbTh\,std}$, etc. Calculation of the partial derivatives yields the following expression for the standard deviation of measured Pb corrected for Th and Y interference:

$$\sigma^2_{Pb,corr,unk} = \sigma^2_{Pb,uncorr,unk} + \sigma^2_{Pb,Thstd}\left[\frac{(-Th_{Th^o std})(Th_{unk})}{(Pb_{Pb\,std})(Th_{Th\,std})}\right]^2 +$$
$$\sigma^2_{Pb,Pbstd}\left[\frac{(Pb_{Th\,std})(Th_{Th^o std})(Th_{unk})}{(Pb_{Pb\,std})^2(Th_{Th\,std})} + \frac{(Pb_{Y\,std})(Y_{Y^o std})(Y_{unk})}{(Pb_{Pb\,std})^2(Y_{Y\,std})}\right]^2 + \sigma^2_{Th,Thstd}\left[\frac{(Pb_{Th\,std})(Th_{Th^o std})(Th_{unk})}{(Pb_{Pb\,std})(Th_{Th\,std})^2}\right]^2 +$$
$$\sigma^2_{Th,Th^o std}\left[\frac{(-Pb_{Th\,std})(Th_{unk})}{(Pb_{Pb\,std})(Th_{Th\,std})}\right]^2 + \sigma^2_{Th,unk}\left[\frac{(-Pb_{Th\,std})(Th_{Th^o std})}{(Pb_{Pb\,std})(Th_{Th\,std})}\right]^2 + \sigma^2_{Pb,Ystd}\left[\frac{(-Y_{Y^o std})(Y_{unk})}{(Pb_{Pb\,std})(Y_{Ystd})}\right]^2 +$$
$$\sigma^2_{Th,Thstd}\left[\frac{(-Pb_{Y\,std})(Y_{Y^o std})(Y_{unk})}{(Pb_{Pb\,std})(Y_{Y\,std})^2}\right]^2 + \sigma^2_{Y,Y^o std}\left[\frac{(-Pb_{Y\,std})(Y_{unk})}{(Pb_{Pb\,std})(Y_{Y\,std})}\right]^2 + \sigma^2_{Y,unk}\left[\frac{(-Pb_{Y\,std})(Y_{Y^o std})}{(Pb_{Pb\,std})(Y_{Y\,std})}\right]^2 \tag{10}$$

Figure 4a shows 102 measurements of uncorrected (x) and corrected (y) Pb counting statistics for monazites from the mid-Proterozoic of New Mexico (Daniel and Pyle, in prep). In general, correction adds very little to the overall uncertainty (+0-0.3%). However, the analyses within the ellipse are all high-Th (≥ 12 wt. %) monazite. The product of high Th counts with high uncertainty (5-7%) in the measurement of apparent Pb in the Th standard increases the value of the second term of the RHS of equation (10), i.e. $\sigma^2_{Pb,Thstd}\left[\frac{(-Th_{Th^o std})(Th_{unk})}{(Pb_{Pb\,std})(Th_{Th\,std})}\right]^2$, by nearly a factor of three relative to value of this term in low-Th monazite, resulting in less precise analyses. Comparison of standard deviations for corrected Pb Mα and interference-free Pb Mβ (Fig. 4b) demonstrates that, with the exception of high-Th (≥ 10 wt. %) monazite, Pb Mα provides a more precise analysis.

***X-ray detector gas and escape peaks*** An in-depth explanation of the role of detector gasses in EMP analysis is presented in Goldstein et al. (1984) and Scott et al. (1995). However, an issue related to detector gas that merits further discussion is escape peak formation, and their effect on monazite chemical age determinations.

Escape peaks are formed in the X-ray detector when an X-ray from the unknown generates a detector gas X-ray instead of an ion-electron pair or Auger electron. There is a high probability of the Ar or Xe X-ray escaping the detector, rather than producing more Ar or Xe ion-electron pairs. Upon X-ray escape, the energy of the output voltage pulse, which nominally corresponds to the energy of the incoming X-ray from the analyzed sample, is reduced by an amount proportional to the energy of the characteristic X-ray of the detector gas, namely 2.96 keV for Ar, and 4.11 keV for Xe. If the energies of the analyzed element (e.g., $E_{Pb\ M\beta}$) and the escape peak (e.g., for a Ce escape peak, $E_{Ce\ L\alpha} - E_{Ar\ K\alpha}$) are similar, potential for escape peaks

to appear in the WD spectrum exists. It should be noted that the voltage pulse produced by the escape peak has no correspondence to any characteristic line energies of the element from which it was produced, but the escape peak voltage, if passed to the detector, will produce a peak in the WD spectrum at a location corresponding to the energy of the original X-ray line, but of diminished intensity.

The phenomenon of escape peak formation in the pulse height analyzer can be understood using virtual pulse height analysis. Figure 5 (a,b) shows virtual pulse height scans generated for $CePO_4$ doped with 0.5 wt % Pb, for both an argon detector (Fig. 5a) and a xenon detector (Fig. 5b) with the spectrometer tuned to the Pb Mβ peak. A number of monazite chemical dating protocols (e.g., Scherrer et al., 2000) select Pb Mβ for analysis, in preference to Pb Mα, due to the significant element interferences affecting Pb Mα, namely Th $M\zeta_1$, Th $M\zeta_2$, Th M2-O4, and Y $L\gamma_{2,3}$. Two points draw immediate attention. First, the Ar escape peak from the second-order Ce $L\alpha_1$ line falls largely within the voltage window occupied by Pb Mβ (Fig. 5a), whereas the Ce Lα (n=2) escape peak in the Xe detector is completely excluded by the voltage window centered on Pb Mβ. This Ce Lα escape peak in the Ar detector cannot be filtered without removing a significant portion of the Pb Mβ signal.

Second, the intensity of the escape peak in the Xe detector is much less than that of the Ar detector escape peak. In general, escape peaks produced in Xe detectors are of negligible intensity (Scott et al., 1995) because: 1) the K-absorption edge of Xe is of much higher energy (34.56 keV) than the range of energies (0-25 keV) encountered in typical EMP analysis; 2) Xe Lα X-rays are more efficiently absorbed in Xe gas than are Ar Kα X-rays in Ar gas.

The WD spectrum produced with the Ar detector (Fig. 5c, grey line) clearly shows the result of the Ce Lα second-order escape peak produced in the detector. The resulting peak is

about 1.5 times as intense as the adjacent Pb Mβ line, and produces significant overlap. The Ce peak is seen in this form in the WD spectrum because the Ce and Pb peaks are not completely resolved by this combination of diffraction crystal and 140 mm Rowland circle. A spectrometer with a higher resolution (e.g. CAMECA's 160 mm Rowland circle)would be expected to produce less overlap, and consequently, less apparent lead due to Ce interference. Likewise, a high intensity (PETH) spectrometer (100 mm Rowland circle), would generate more overlap (less peak resolution), and a higher apparent, Ce-derived, lead concentration.

The quantity of the Ce Lα (n=2) - Pb Mβ overlap has been calculated by measuring the apparent amount of lead in Pb-free $CePO_4$ (synthesized by E. B. Watson) at the Pb Mβ position. Analysis of this $CePO_4$ (~ 60 wt. % Ce) on the JEOL 733, using a PET crystal with an Ar detector, yields an apparent lead concentration on the order of 400-500 ppm. With the exception of grains enriched in huttonite or brabantite component, a typical metamorphic monazite contains 25-28 wt. % Ce, equivalent to 200-250 ppm apparent lead, due to Ce Lα (n=2) interference on Pb Mβ. This is an interference that is nearly independent of U, Pb and/or Th concentration. For a 300 Ma monazite with 5000 ppm U and 4 wt. % Th (~750 ppm Pb), this interference produces an apparent age increase of roughly 80-100 Ma for monazite of average. For monazites of 300 Ma or younger, and typical U and Th compositions (as above) this generates a *minimum* inaccuracy of ±25-33 %.

This analysis may be extended to all high- to moderate- concentration REE and actinides present in monazite. For Ar detectors optimized for Pb analysis, the escape peaks that appear in the WD spectrum are those of the second-order LREE-MREE (La-Eu), Th, and U. For Pb Mα analysis with an Ar detector, the second-order La Lα escape interferes with Pb Mα, but due the separation of Pb Mα and La Lα, the magnitude of the interference is negligible. However, if

voltage windows are run in integral (wide) mode, then the full intensity of the second order La Lα is passed to the counter (see below), and a correction for La Lα interference on Pb Mα must be made in a manner analogous to the Ce Lα (n=2) - Pb Mβ correction.

For Xe detectors optimized for Pb analysis, the escape peaks that appear in the WD spectrum are the third-order MREE-HREE (Nd-Er). Because of the much lower concentrations of MREE and HREE in monazite, plus the lower intensity of escape peaks produced in Xe detectors, the contributions of third-order MREE-HREE escape peaks to potential interferences along a monazite WD spectrum are negligible. The spectrum produced with a Xe detector (black line, Fig. 5c) does not show the second-order Ce peaks. Because the Ce $L\alpha_1$, Ce $L\beta_{1,4}$ and Ce $L\beta_{2,15}$ second order lines are greatly diminished, the background produced with a Xe detector is flatter, and no correction is necessary for Ce interference. In a xenon-detector WD spectrum of a natural monazite, the $L\alpha_1$, $L\beta_{1,4}$ and $L\beta_{2,15}$ lines of La and Nd are diminished correspondingly.

***X-ray collimator setting*** Adjustable X-ray collimators decrease the divergence from the Bragg angle for X-rays impinging on a diffraction crystal. X-ray collimation increases peak-to-background ratio by narrowing peaks and diminishing the intensity of background radiation. This has the effect of decreasing elemental detection limits. However, collimation also decreases overall intensity, and thus reduces analytical precision. It is therefore instructive to examine monazite spectra at different collimator settings to determine which settings maximize peak-to-background ratio while minimizing peak overlaps.

Figure 6 shows a series of WD scans of Trebilcock monazite (Tomascak, 1996). Scans were acquired simultaneously with PET crystals on Ar and Xe detectors, at open (3 mm) setting (Fig. 6a), 500 μm setting (Fig. 6b), and 300 μm setting (Fig. 6c). Second-order LREE peaks are present on all Ar detector scans (top line, Figs. 3a-c), but are absent on Xe detector scans (bottom

line, Figs. 6a-c). The most noticeable difference between the Ar and Xe spectra occurs with the collimator at the open setting (Fig. 3a). There is a moderate concave-upwards curvature in the Xe-scan background, and a pronounced concave-upward curvature in the Ar-scan background; background curvature is moderately to greatly reduced with narrower collimator settings (Figs. 3b,c). Additionally, there is a "hump" in the background of the Ar-detector spectrum between 165-153 mm that is absent from the corresponding Xe-detector spectrum (Fig. 3a). This phenomenon is not a function of fluctuating current during the 24 minute scan, as the current for all three scans, shown by the dotted lines (Figs. 3a-c) does not vary by more than 2 % relative over the course of the signal collection. This "hump" may be due to a combination of X-ray scattering and detector response over this wavelength. Ar-detector, open-collimator WD scans on PET of elementally simple materials such as quartz, aluminum, and kyanite show pronounced upward background concavity over the same spectrometer working-distance interval. The absence of this feature on the Xe-detector spectrum, and its diminishment at narrower collimator settings on the Ar detector, suggests that this phenomenon is a combination of Ar ionization potential over this wavelength, coupled with detection of a large range X-ray wavelengths due to Johann (1931) focusing and/or detector crystal warping or degradation. The existence of this hump also renders monazite background placement for this combination of collimator setting and detector gas virtually impossible.

Table 3 lists peak to background ratio and analytical precision of Pb Mα, Pb Mβ, and Ce Lα (second order) for all six spectra, and the variation in peak counts and peak to background ratio for the lead peaks is depicted graphically in Figure 7. Peak intensity, and thus precision, increases with increasing slit width (Table 3, Fig. 7a), so the maximum X-ray collimator width is

favored for this reason. However, the Ar spectra with a 3 mm slit width is unusable, for reasons stated above.

***Background placement*** The combination of Ar detector gas ionization efficiency and the generation of LREE second order escape peaks makes two-point background placement for monazite spectra problematic. Figure 8a shows a portion of a WD scan of Trebilcock monazite using an Ar detector and PET crystal. Second-order escape peaks of Ce, La, and Nd are visible, and the significant curvature of the background requires either: 1) background positions close to analyzed lead peak, if a two point background is to be used, to interpolate background counts under the peak, or; 2) an exponential fit to background if background points are far removed from the peak. If background points are spaced far apart, the interval will subtend a curved portion of the background. The presence of the Ce Lα peak in the Ar scan restricts placement for Pb Mβ high background to a region to the high side of the Th $M\zeta_2$ peak, and likewise restricts placement of Pb Ma low background to a region to the low side of Th M4-N3 peak (Fig. 8a). The curvature between these two background points essentially requires modeling of the background region with an exponential function.

However, use of a Xe detector (Fig 8b) eliminates the second order Ce Lα escape peak, and also slightly diminishes the curvature of the background. This allows the same location to be used for both the Pb Mβ high background and the Pb Mα low background(Fig. 8b), significantly decreasing the inter-background separation. With the background positions shown (Pb Ma: +6.27 mm high, -3.90 mm low; Pb Mb: +2.83 mm high, -2.40 mm low), a two-point background collection with linear interpolation is adequate to obtain background intensity at the peak position.

**Discussion of Precision**

To this point, all factors directly related to analytical precision have been selected so as to yield the lead analysis with the highest possible precision. Analyzing Pb Mα on a xenon X-ray detector with X-ray collimator at maximum width maximizes lead signal intensity, while removing potentially interfering second order LREE escape peaks (notably Ce Lα), as well as decreasing background curvature. Furthermore, the decrease in precision for interference-corrected Pb Mα analyses is, unless the monazite in question is highly (> 10 wt. %) enriched in Th, still more precise than interference-free Pb Mβ analysis performed on a Xe detector. The magnitude of interference corrections is variable, and depends primarily on Pb content, which is function of both age and actinide concentration. Table 4 shows uncorrected and corrected ages for both Proterozoic (00-2A, 94-27) and Paleozoic (BF-64, TM-637, Trebilcock) monazites; the magnitude of the correction is 1-2 % relative for the Proterozoic monazites, and 10-15 % relative for Paleozoic monazites.

Combination of Pb Mα analysis and a xenon detector maximizes analytical precision for the JEOL 733; attainment of the desired analytical precision for this combination of lead peak and X-ray detector is a function of analytical time and current. For the JEOL 733 Superprobe at RPI, an intrinsic detector response of ~0.33 counts Pb/sec•nA•wt.% Pb is measured at 200 nA with a PET crystal and a xenon detector. Figure 9 shows calculated Pb analytical precision for this detector response, and a measured detector response of 0.11 counts/sec•nA at hi and low background positions, for Pb concentrations of 10000 ppm, 1500 ppm, and 250 ppm. For a counting time of 10 minutes on peak and 10 minutes on background (dashed line, Fig. 9b) 1-sigma counting errors of 12%, 2%, and 0.5 % are achieved for the 10000 ppm Pb, 1500 ppm Pb, and 250 ppm Pb monazites, respectively. These uncertainties translate to 2-sigma (95%

confidence level) compositional uncertainties of ±2 ppm Pb, ± 11 ppm Pb, and ± 60 ppm Pb, respectively.

For analyses performed on the RPI JEOL 733 Superprobe (Daniel and Pyle, 2002, in prep; Spear et al., submitted; Pyle et al., this volume), analytical precision for Th Mα is generally at or smaller than 1 %; U Mβ precision typically ranges from 1.5 to 3.0 %, with a negligible loss of precision after correction for Th Mγ interference. Pb Mα precision averages 1-4 % (±70-150 ppm Pb) for ~1420 Ma monazite from the Proterozoic of New Mexico (Daniel and Pyle, 2002), 3-5 % (±70 ppm Pb) for Th-rich Trebilcock monazite, and 3-18 % (±60-100 ppm Pb) for metamorphic monazite from the Acadian of central New England (Spear et al., submitted, Pyle et al., this volume). The overall precision of the age estimate can be approximated by the square root of the sum of the squares of the individual precisions of the U, Th, and Pb analyses (Bevington, 1969). This approximation yields 1-sigma age precisions of roughly ±42 Ma (±3 %) for ~1420 Ma New Mexico monazite to ±52 Ma (±15 %) for 350 Ma Neo-Acadian monazite from New England.

If monazite analyses are drawn from a single age population, it is expected that the mean age, barring systematic errors, will approximate the true monazite age, and the variation of the age estimates about the mean age will be described by the sum precision of U, Th, and Pb analyses, as described above. If the ages are normally distributed about the mean, approximately 95 % of the age determinations will lie within ±2σ of the mean age. However, the precision of *repeated* measurements of the average age of monogenetic monazite – the mean of the average - is described by the standard error of the mean. For N determinations of a mean age with standard deviation σ, the standard error of the mean equals $\sigma/\sqrt{N}$. Figure 10 is a frequency histogram, with a bin size of 50 ppm Pb, showing the relationship between measured data, the mean of the data

and associated probability distribution, and the distribution of the means (standard error) for a group of Pb Mβ concentration measurements on Trebilcock monazite (measurement of Pb Mβ was used in an analytical protocol superceded by the one presented here). For analysis conditions (200 nA, 180 sec), the 1-σ standard deviation associated with analysis of Pb Mβ is roughly 5-7%, which translates into compositional standard deviation of 75-100 ppm lead, or ±12-16 M.y. age uncertainty, regardless of the number of analyses. However, if an analyzed grain population is shown to be monogenetic by application of various statistical tests (Wendt and Carl, 1991; Montel et al., 1996; Cocherie and Albarede, 2001), then the standard error is as the range within which the means of separate groups of measurements within the grain are expected to vary, and a *maximum* estimate of the precision to which the monazite crystallization age is known. For a group of 10 measurements of Trebilcock Monazite (Fig. 10a), the standard error is 1.75 % (1-σ), which translates into a reproducibility of ±26 ppm, or ± 5 M. y. Increasing the number of measurements to 90 (Fig. 10b) decreases the standard error to 0.7% (1-σ), or ± 10 ppm (± 2 M.y) reproducibility. Thus, if all machine conditions are reproduced perfectly, the 95 % confidence interval (2-σ) for the distribution of the mean is ±4 M.y., roughly 2 % of the age of monazite crystallization (~285 Ma).

Multiple domains may be recognized within a single monazite grain, and separated on a compositional, textural, or age basis. In some cases, individual monazite domains are repeated in a systematic fashion across grains in a sample or sample suite, and these domains may be correlated with specific monazite forming events (Pyle and Spear, 2003). In such situations, if separate domains are identifiable on a petrologic, chemical, or textural basis, the precision to which the average age of each domain is known is described by the standard error of the average age of the domain. Pyle and Spear (2003) identified four separate monazite growth events in

low-pressure migmatites from SW New Hampshire, USA. The histogram of monazite age distributions (Fig.11a) approximates a normal age distribution with a mean age of approximately 380 Ma, and a standard deviation of ±30 Ma, but zones 1-4, each correlated with a specific monazite forming reaction, represent a chronological sequence of mutually distinguishable monazite growth events, with standard errors on the order of 3-6 Ma for each domain (Fig. 11b).

## ANALYTICAL PROTOCOL

### Sample Preparation

Use of lead-free polishing media is essential in preparation of monazite for chemical dating, as lead-bearing polishing disks deposit lead within cracks and along grain boundaries. Use of Pb-free laps, as described by Scherrer et al. (2000), remove the risk of sample contamination during polishing. An alternative to mechanical polishing of monazite is chemical mechanical polishing using a colloidal silica suspension. The high pH (9-10) of the suspension enhances sample surface reactivity, and suspended silica particles with a size distribution of 0.05-0.07 μm impart an ultra-high quality polish. CMP polishing produces an exceptionally flat grain boundary polish (Figs. 12a, b), and is ideal for polishing of grain-boundary alteration features (Fig. 12c). After polishing, sample is sonicated, cleaned with isopropyl alcohol, and dried at 60-80°C for 12-24 hours to drive off adsorbed water in fractures and other surface asperities, prior to carbon coating.

### Standard Selection

Standards for the elements U, Th, Pb, Y, and Ce are required for this monazite dating protocol. Standard selection for monazite analysis is discussed at length in Scherrer et al. (2000) and Pyle et al. (2002); the latter address standard selection with respect to the magnitude of ZAF corrections generated by a particular standard set and unknown. A typical monazite varies

greatly in U, Th, Y, and especially Pb concentration with respect to standard materials for these elements. As this standard-unknown compositional disparity can not be minimized, since standards with trace levels (< 1 wt.%) of U and Pb are impractical, the most important consideration becomes accurate characterization of standard composition. For this reason, we standardize with well-characterized synthetic standards including $CePO_4$, $YPO_4$, $ThSiO_4$, $UO_2$, and $PbSiO_3$ (Table 5). $PbSiO_3$ has an additional advantage in that, for typical monazite compositions, it generates slightly smaller $ZAF_{unknown}/ZAF_{standard}$ ratios than crocoite or pyromorphite (Pyle et al., 2002).

A monazite with accurately characterized U, Th, and Pb concentrations also serves as a chemical age standard. To date, however, no such monazite with precisely and accurately determined U, Th, and Pb concentrations has been synthesized for this purpose. In lieu of a primary chemical age standard, many protocols (Williams et al., 1999; Scherrer et al., 2000) employ a monazite secondary age standard that has been characterized by conventional analysis, compositional and age mapping (e.g., Williams et al., 1999), and single-grain or *in-situ* U-Pb or Th-Pb isotopic analysis. The secondary age standard used at RPI is a monazite from the Trebilcock pegmatite quarry, Topsham, Maine. Trebilcock monazite gives slightly reversely discordant TIMS ages of 271-277 Ma ($^{207}Pb/^{235}U$), and $^{206}Pb/^{238}U$ ages of 279-285 Ma (Tomascak et al., 1996).

**Detector Electronic Settings and Pulse Height Analysis**

The role of detector electronics in shaping and filtering voltage pulses passed to X-ray counters is discussed at length in Goldstein et al. (1984) and Scott et al. (1995). Essentially, detector gain and bias settings are adjusted so that when the spectrometer is tuned to a particular X-ray line, the voltage pulse produced by X-ray ionization of the detector gas is centered in the

SCA voltage window. Voltage windows are typically run in differential (narrow) mode so as to filter unwanted, higher-order reflections, A narrow voltage window for Pb Mβ analysis in monazite (Fig. 5b) filters the second-order Ce Lα peak, and narrow windows for Pb Mα analysis filter the second-order La Lα peak.

Adoption of narrow voltage windows for pulse height analysis, however, has the potential to generate a separate analytical problem relating to voltage pulse shift. Voltage pulse distributions shift to lower voltages if count rates substantially increase, or to higher values upon a significant count rate decrease, for reasons addressed by Goldstein et al. (1984). Count rate is proportional to analysis current, so pulse shift can be generated by large changes in current.

Typically, calibration and analysis are performed at the same beam current (Scherrer et al. 2000, and references therein) of high value (50-250 nA) to maximize lead analytical precision. In the case of an element present at trace element levels in the unknown, and at high concentration in the standard, the potential exists for a pulse shift to higher voltages, due to a significant count rate decrease. Setting narrow voltage windows based on calibration PHA may result in cut-off of some higher-voltage lead signal during analysis. To prevent cutoff of high voltage pulses (i.e., Pb signal), calibration current can be significantly lowered (e.g., from 200 nA to 10 nA) to minimize count rate change.

Adoption of low calibration current minimizes the chances of Pb signal clipping, but does leave the potential for voltage clipping of elements present in high concentrations in natural monazite, such as Ce or Th. Ce concentrations in natural monazite are typically ~50 % of the Ce concentration in $CePO_4$, and Th concentrations in metamorphic monazite may approach 15-30% of the concentration level of Th in $ThSiO_4$. For the example shown in Figure 13, setting the voltage windows around the Ce pulse generated during calibration (Fig. 13a) results in the loss of

10 % of the Ce signal generated during analysis (Fig. 13b). In high-Th (≥ 15 wt. %) monazite, setting minimum width windows during calibration resulted in clipping of 3-5 % of the Th signal from the unknown.

Voltage windows should be set sufficiently narrow to filter higher-order peaks, yet wide enough to absorb possible pulse shift without clipping signal. This requires estimating the count rate range for all elements during calibration, measurement of correction factors (Th, Y) and analysis. Table 6 lists calibration, correction measurement, and analysis count rate ranges for elements measured on the RPI JEOL 733 Superprobe.

**Variable background settings**

Xenon detectors remove second-order LREE escape peaks, and produce spectral backgrounds with slightly less curvature than argon detectors, enabling use of two-point background with linear interpolation (Fig. 8). However, there is significant difference in spectral form between monazite standards (Fig. 3) and natural monazite (Figs. 5, 6, 8) due to: 1) increased concentration of elements in standard materials, and; 2) compositional complexity of natural monazites relative to standard material. Therefore, the positions chosen for background collection in the unknown may not be the optimal positions for collection of background in the standard material, or vice versa. Therefore, we advocate switching background collection positions between calibration and analysis of unknowns. Background collection positions (given as high and low offsets from elemental peak position) for calibration and analysis are given in Table 7, along with other calibration and analysis settings.

**Calibration and analysis conditions**

It is recognized that there is no one perfect monazite chemical dating protocol, as selection of optimal analysis conditions is sensitive to monazite size, morphology, composition,

and chemical zonation, all of which are highly variable. However, the protocol presented below optimizes Pb precision in all but extreme (e.g., high Th or U) or unusual (e.g., S-rich) monazite compositions.

***Accelerating voltage*** A survey of the literature (Scherrer et al., 2000, and references therein) shows accelerating voltages range from 15-25 keV; we have adopted an accelerating voltage of 25 keV. Scott et al.(1995) suggest adoption of accelerating voltages of 2-3 times the critical excitation energy of the analyzed element. for a given current and analysis duration, higher accelerating voltages increase X-ray intensity and analysis precision. Higher beam energies also increase excitation volume, but this increase is offset by the higher average atomic number (Z~40) of monazite, so that excitation volume during analysis of monazite at 25 keV should not exceed a radius of ~ 2 μm (Goldstein et al., 1984). The only other negative effect is a large ZAF correction associated with large over voltages (beam energy minus critical excitation energy) for the M lines of Pb, U and Th ($E_{critical}$ 2.5 – 3.5 keV).

***Sample current and beam size*** Published monazite analytical protocols (see Scherrer et al., 2000) call for analysis currents of 10 nA to 250 nA. A number of trials were performed on Trebilcock monazite, and assessment of analytical precision and sample damage resulted in adoption of an analysis current of 200 nA for this protocol. To delay the onset of beam burn through at this current, the electron beam is defocused slightly to 5-7 μm. This defocusing allows most monazite grains to withstand 3-5 same-spot cycles of a 6-minute analysis (3 minutes Pb peak, 3 minutes Pb background) cycle at 200 nA, which increases precision by a factor of $\sqrt{3}$ to $\sqrt{5}$ over a single cycle. However, analytical domains of less than 5 μm diameter can not be sampled separately from adjacent domains with a slightly defocused beam. In such as case,

the beam can be focused to spot size (1-2 μm), but the grain surface may survive only one cycle before burn through.

***Analysis duration*** Given the intrinsic detector response measured on the JEOL 733 Superprobe (Fig. 9), a single Pb analysis cycle of 3 minutes peak plus 3 minutes background yields analytical precisions of ~3% at 1500 ppm Pb, and ~15% at 250 ppm Pb. In the case of low lead concentrations (≤ 500 ppm) multiple analyses are performed on a single spot.

**Other in-analysis issues**

***Element Mapping*** Heterogeneous distribution of monazite compositional domains can correspond perfectly to heterogeneous age domains (Williams et al., 1999), and/or the compositional domains may relate to individual whole-rock events or reactions (Pyle and Spear, 2003, each with a definable mean age and variation described by the standard error of the mean age. As such, monazite element and/or age maps provide useful guides for individual grains. Monazite grains are usually mapped at a current of 200 nA or greater, and Th and Y are typical domain differentiating elements.(Williams et al, 1999; Pyle and Spear, 2003).

***Spectrometer drift*** Jenkins and Devries (1982) show that significant thermal expansion of PET can occur for even modest temperature changes (Fig. 14a). Pb Mα, at a two-theta of approximately 35.2° for PET, is particularly prone to peak shift; a change of 5°C in ambient temperature results in a calculated peak shift of at least 0.025° two-theta. This translates to a peak shift of approximately $D_{Rowland}$ of 0.1 mm, and as measured on the JEOL 733, a loss of approximately 20 % of previous peak counts. Decreases of 3-7% in Pb k-ratio during analysis indicate that the temperature shift, if responsible for peak drift, is on the order of 1-2°C. This observation underscores the importance of climate control in the space housing any EMP used for chemical dating of monazite.

Intermittent monitoring of lead standard k-ratios plus Th and Y interference correction factors indicate whether the Pb calibration has held, or if focus or spectrometer drift has occurred since the beginning of the analytical session. Figure 14b shows a series of k-ratio measurements on the lead standard $PbSiO_3$ over a three hour period. Over this time, the average k-ratio has decreased by roughly 2 %, meaning that the final measured unknown Pb concentrations are 2 % less than if they had been measured just after calibration. If drift is apparent, lead concentrations must be drift-corrected (Appendix 1).

***Correction factors*** Correction of Pb Mα for Th and Y interference, and correction of U Mβ for Th interference, require measurements of the apparent Pb concentration in the Th and Y standards, and measurement of apparent U in the Th standard. If Pb Mβ is measured, especially if an Ar detector is used, then apparent lead must be measured in the Ce standard to correct for interference of second order Ce Lα. Correction factors should be measured at the beginning of the session, just after calibration. using analysis current (200 nA) and background positions. Ideally, three to five measurements of each correction factor (eq. 4) are made and pooled to produce an average value for the correction factor.

## ACCURACY OF MONAZITE CHEMICAL AGES

Currently, evaluation of the accuracy of monazite chemical ages in a rigorous fashion is impossible, due to the lack of synthetic monazite chemical age standards with known concentrations of U, Th, and Pb. Systematic errors in monazite chemical dating, however, can be identified, classified as machine-related and sample related, and the contribution of each systematic error can be quantified or semi-quantified, and summed, in order to estimate the magnitude of deviation from the "true" age, over and above that associated with statistical

uncertainty. Sources of inaccuracy, both machine- and sample-related, are listed in Table 8, and treated in detail below

**Quantifiable sources of Inaccuracy**

***Poorly characterized monazite standards*** Reports of lead contamination of nominally pure $REEPO_4$ standards have been collected and confirmed by Donovan et al. (submitted). LREE phosphates synthesized with a lead pyrophosphate flux ($Pb_2P_2O_7$) commonly contain between 0.5 to 4.0 wt. % Pb replacing REE. If $CePO_4$ is used as a Ce standard for chemical dating, the assumed Ce concentration in the standard may be in error by the above concentration, or if Ce is fixed during analysis, the amount entered for the ZAF or $\phi\rho z$ correction matrix will be in error a like amount. However, variations in fixed values for matrix corrections affect chemical ages to a negligible degree (see below), so contaminant lead in REE phosphate standards introduces inaccuracies of magnitude less than those associated with counting statistics.

***Dead time*** Typical detector electronic dead time for WDS systems is on the order of 1 μs (Scott et al., 1995); many current counter systems, such as the Self-Contained Pulse Processing System (Geller Micro analytical) in use in the JEOL 733, employ live-time digital correction that minimizes dead time effects (maximum ±2%) for count rates of up to 200,000 cps. For the range of counts typical of monazite calibration, correction for element interference, and analysis (Table 6), detector dead time should introduce negligible error to monazite chemical ages. Measurement of yttrium for the Y-Pb interference correction factor is prone to dead time effect; yttrium k-ratios of 0.95 to 0.97 measured on $YPO_4$ at 200 nA are common. However, as yttrium interference corrections are generally in the 10-100 ppm range, the additional error of 0.5 –5.0 ppm in the Y correction factor is not resolvable by EMP analysis.

***Voltage pulse shifts*** As previously mentioned, loss of counts from voltage pulse clipping of high concentration elements could occur if special attention is not paid to voltage window settings. Losses of 3-5 % can occur in Th-rich samples with a minimum voltage window width set during calibration. The loss of Th signal translates to a 3-5 % increase in apparent age.

***Peak drift*** Changes in standard intensity over time due to temperature effects have been demonstrated (Fig. 14). The drift may produce a positive or negative change in standard intensity, and the drift may be continuous or punctuated. A spectrometer drift corresponding to an apparent 2 % loss in lead content after 3-plus hours is shown in Fig. 14, and drifts of greater magnitude (5-7 %) have been observed over the course of longer analytical sessions (Appendix 1).

***ZAF corrections*** The quantification program dQant32 (Geller Micro analytical) used in conjunction with the JEOL 733 Superprobe at RPI allows user selection of different ZAF correction schemes, including Armstrong (1984), Heinrich (1985), Love/Scott (Sewell et al., 1985), Basting et al.(1984), and Dumdum and Reed (1968). Each of these correction routines was applied to an analysis of Trebilcock monazite pre-corrected for element interference (Table 9, Part I). The total variation in Pb concentration, ~50 ppm (Table 9), is less then the variation in Pb due to single-point 1-sigma counting statistics, approximately ±85 ppm (Figure 15a). Likewise, the spread in age encompassed by the different correction schemes (~15 M.y.) is less than the age uncertainty associated with Pb counting statistics, and approximately equal to the total (U+Pb+Th) compositional uncertainty (~15 M.y., 1-sigma) due to statistical fluctuations (Figure 10b). Thus, the error introduced by selection of different ZAF correction routines is no larger than the error associated with statistical error.

The effect of elemental variation in monazite on resultant ZAF corrected U, Th, and Pb concentrations can be assessed by singly varying concentration of elements normally fixed (Table 1) during monazite chemical age analysis. Part II of Table 9 shows the result of varying fixed element concentrations (La, Ce, Pr, Nd, Sm, Gd, Y, P, and O) by at least 2 standard deviations of the average monazite composition reported in Table 4. The ages generated by changes in calculated U, Pb, and Th concentrations arising from varying nominally fixed LREE concentrations vary by only 1 M.y.

**Non- or semi-quantifiable sources of inaccuracy**

***Sample damage*** Williams and Jercinovic (2002; this volume) have noted permanent "spotting" of analyzed monazite surfaces, which are associated with a decrease in phosphorus concentration. Bubbling of carbon coats and associated decrease in absorbed current are also noted for long analysis times. First-order calculations of thermal conductivity of carbon-coated and/or gold-coated monazite surfaces exposed to high-current electron beams show significant temperature increases of $\geq$ 1500 K (M Jercinovic, pers. comm.). Monazite melting requires a grain surface temperatures in excess of 2000°C (Boatner and Sales 1988; Boatner, 2002). Evaporation of adsorbed or structural water and loss of carbon coating, with concomitant drop in both absorbed current and X-ray counts, occurs at much lower temperatures. In this study, beam damage has been noted to occur more frequently, and with less beam exposure time, in the Th-rich portions of zoned monazite. Different monazites in the same sample can react quite differently to identical analysis parameters, as Figure 16 shows. Each of two spots in both grains experienced roughly 14 minutes of beam exposure; the grain in Fig. 16a shows only minor spotting, whereas the grain in Fig. 16b appears to have melted. The presence of adsorbed water in the fracture cutting grain b may have fluxed melting.

Th, U, and Pb do not appear to show same-spot, multiple-analysis variations in concentration outside of statistical fluctuation, unless absorbed current changes significantly. Yttrium concentration fluctuation may also be affected by changes in absorbed current. Figure 16c shows a pair of multi-cycle, same spot analyses. Sample damage can be tracked by changes in absorbed current (numbers in italics, Fig. 16c), and also fluctuations in measured yttrium concentration. which, unlike lead, are outside of expected statistical deviation. The change in corrected Pb concentration due to fluctuation in yttrium content is less than associated lead analytical precision. for analysis group II, (Fig. 16c), the maximum change in the Y interference correction is 25 ppm Pb, compared to a standard deviation of ~8 % (~70 ppm Pb) on the overall analysis. Thus, despite the appearance of sample damage and/or fluctuations in absorbed current, significant variations in measured Y concentration do not, in general, affect corrected Pb concentration above statistical uncertainty associated with lead analysis.

***Grain size, orientation, and homogeneity*** If a grain of monazite is small relative to beam size ( $\sim \leq 7$ μm), then all analyses performed on that grain are essentially edge analyses. Such analyses have the potential to be influenced by spectrometer orientation. Additionally, subsurface inclusions, or compositional heterogeneities smaller than electron-beam resolution may also affect chemical age analyses.

Figure 17 shows a schematic cross section of a monazite grain with adjacent matrix phases, and an sub-surface inclusion in monazite. The two spectrometers are separated by an angle of approximately 180°. Electron beam 1 generates excitation volume 1, and while X-rays from volume 1 reaching spectrometer B1 pass entirely through monazite, X-rays reaching spectrometer A1 pass largely through the adjacent grain. Common pelite matrix phases such as quartz, micas, and plagioclase have markedly different atomic numbers and mass absorption

coefficients than monazite, and as such, the collected X-rays (U, Th, Pb) will be corrected for monazite atomic number and mass absorption effects, when in fact the atomic number and mass absorption corrections for the matrix phase should apply. Likewise, X-rays from excitation volume 2 reaching spectrometer A2 will pass largely through monazite, whereas the X-rays reaching spectrometer B2 will pass largely through the subsurface inclusion in monazite, once again rendering ZAF correction factors for monazite non-applicable.

A series of traverses on Trebilcock monazite mounted in epoxy (Figure 18) were performed to test whether spectrometer orientation relative to traverse orientation has any effect on calculated k-ratios and concentrations. Spectrometer orientation is shown at the upper part of each panel. The grain was rotated approximately 60° for each set of line traverses, which included a line in the center of the grain, a traverse parallel to the grain edge, and a traverse perpendicular to and crossing over the grain edge. For example, in traverse 4 (Fig. 14b), X-rays reaching spectrometer 2 will pass largely through the monazite grain, whereas X-rays reaching spectrometers 3, 4, and 5 will pass largely through epoxy.

These traverses (Figure 19) show that if the X-ray path to the spectrometer passes through epoxy, the apparent concentration will increase as the grain boundary is approached. For traverse 4, the X-ray travel path to spectrometers 3, 4 and 5 pass through epoxy, and apparent Pb, as measured by these spectrometers, increases dramatically towards the grain boundary. The same orientation applies for traverse 5, as well. For traverse 8, the X-ray travel path to spectrometer 3 is largely through monazite, and the apparent concentration of Pb as measured by spectrometer 3 decreases, whereas the apparent Pb concentration as measured by spectrometers 2, 4, and 5 increases. In general, any X-ray travel path that reaches the spectrometer through a material with smaller Z and A corrections than those of monazite (quartz, mica, etc.) will result

in an increase in apparent Pb (or Th and U) concentration. The magnitude of the change is severe for a monazite-epoxy grain boundary; traverse 4 displays an apparent Pb concentration increase of 66%, traverse 8 displays an increase of 100%, and traverse 8, 133%. While these increases are extreme because epoxy is highly transparent to X-rays, monazite X-rays passing through quartz at grain boundaries or quartz inclusions may experience a diminished equivalent (~2-5%) of the monazite-epoxy phenomenon. The x-rays of all elements present will be affected, but to different degrees, based on the mass absorption coefficients of the individual element X-rays for the specific non-monazite absorber, and the overall form of the ZAF or $\phi\rho z$ correction. An estimate of the error introduced to chemical age estimates by this effect is speculative unless the process is modeled within a ZAF or $\phi\rho z$ correction, including mass absorption coefficients and other relevant input data for both the presumed and actual absorbers. Monazite grains displaying complex zoning may be cryptically zoned in Th, U, or Pb on a scale smaller than the resolution of the electron beam. This fact, combined with small grain size and/or orientation factors, may lead to inter-spectrometer age variation greater than the expected statistical deviation.

Given typical monazite grain size, morphology, and tendency to include other phases, an ideal monazite analysis excluding edge effects or inclusion effects may be difficult to realize, especially in low-grade samples where monazite grains are commonly small, embayed, and inclusion-rich (Spear and Pyle, 2002, and references therein). Additionally, quantifying these effects may not be possible in a rigorous fashion but recognition of the existence of these factors may help, in part, to explain, and subsequently discard, monazite EMP analyses that produce unusual ($>3\sigma$) or spurious ages.

**Overall Accuracy**

Systematic errors including machine-related (spectrometer drift, pulse shift, dead time) and sample-related (sample damage, size/orientation/composition effects, ZAF corrections) issues can affect the calculated monazite chemical age quite dramatically, especially if the errors are additive. In a worst case scenario, for example, additive errors from Th pulse clipping (5-7% loss of Th), temperature change and resulting increase in lead k-ratio (5-7%), and monazite grain edge effects resulting in artificially boosted lead concentration (5-7%) systematically increase the apparent age 15-20%. This is in addition to random fluctuations about the true age, which are largely dependent on Pb counting statistics, and also assumes: 1) that standard compositions are known perfectly, and; 2) that interference corrections are performed correctly.

However, inaccuracy from systematic errors can be greatly reduced by performing pulse height analysis for all measured elements on both standards and individual compositional domains in natural monazite, and periodic monitoring for spectrometer drift during analysis, with subsequent correction. If pulse clipping is eliminated and spectrometer drift corrected, the remaining systematic errors (deadtime, error/uncertainty in ZAF correction models, imprecise knowledge of standard composition, sample damage effect on measured composition) add a maximum of 1-2 % each, or 4-8% total, uncertainty to the statistical variation of the analysis. Furthermore, suspect analyses may be discarded if: 1) large changes in absorbed current result in multi-analysis, same-spot compositional variation of greater than $2\sigma$, or; 2) edge, size, orientation, or inclusion effects may introduce spurious ZAF corrections.

## DISCUSSION

Inasmuch as there are currently no chemical monazite age standards, the favored method of evaluating chemical monazite ages is by comparing chemical and isotopic monazite ages for the same grain. The implicit assumption of this comparison is that reproduction, within analytical uncertainty, of isotopic monazite ages by chemical monazite dating, indicates a "correct" chemical age analysis. However, the potential exists for analytical discordancy in monazite Th/Pb and U/Pb isotope ages (Spear et al., submitted), so no one monazite dating method should be unilaterally viewed as giving the "correct" answer. Isotope dating methods do have the advantage of much greater single-spot analytical precision, at least for U/Pb and Th/Pb ages, but this is subject to the potential analytical discordancy mentioned above. For this reason, comparative monazite isotope analyses presented below quote $^{207}Pb/^{206}Pb$ ages

Williams et al. (1999, Fig. 1) found excellent agreement between published monazite isotope ages and their chemical age analyses of monazites from the same samples, for an age range of 300 to 2600 Ma. Terry et al. (2000) concluded that monazite chemical ages of 397±4 Ma and 408±6 (average ± 1 standard error of the mean) for domains "a" and "b" from his ultra high pressure eclogite sample UHP 1 (Western Gneiss Region, Norway) were statistically indistinguishable from SHRIMP ages of 398±6 Ma and 415±7 Ma (average + 1 standard deviation) of the same domains.

For our comparison, we present chemical and isotopic analyses of a large monazite inclusion in garnet from aluminous schist of the Cavendish formation, Star Hill, VT, USA. Further analytical information on this and associated samples is presented in Spear et al. (submitted). The monazite is several hundred μm long, and has two distinguishable chemical domains; a core region of low Th (2-3 wt. %) and U (0.3-0.5 wt. %) overgrown by a

discontinuous rim of high Th (~6-9 wt. %) and U (1-2 wt. %) (Fig. 20a). Fifty single-cycle spot chemical age analyses were performed on this grain (Fig. 20b), yielding 100 ages, and the compositions, with associated calibration information, correction factors, ages and statistical uncertainties, are given in Table 10. Isotopic analysis information for this grain is presented in Table 11. Details of analytical protocol, including interference and drift correction, are presented in Appendix 1.

Analytical precision (Table 10) for lead ranges from 7-15 %, or 17-34 Ma (1σ) for core analyses, and 3-7 %, or 13-17 Ma (1σ) for rim analyses. Average chemical ages for the core (418±41 Ma, n=62, 1σ) and rim (419±25, n=38, 1σ) are indistinguishable, and the rim domain yields a slightly lower standard error (±4 Ma), than the core domain (± 6 Ma). The age distribution for the whole grain (Fig. 20c) is reasonably well approximated by a normal age distribution with a mean age and standard deviation equal to that of the core domain. As a whole, the overall distribution of $^{207}Pb/^{206}Pb$ ages (Table 11) agree with chemical ages (Fig. 20d), though the average $^{207}Pb/^{206}Pb$ age of the rim domain of 392±18 Ma (1 s.e.) is younger than the average rim chemical age, but still within error; the average $^{207}Pb/^{206}Pb$ age of the core domain (423±13 Ma, 1 s.e.), is nearly identical to the core domain chemical age (418±41 Ma, 1σ). The cause of the older rim age in the chemical analyses is unknown, but may be related to systematic underestimation of chemical ages associated with very high U and/or Th content.

Optimization of lead analytical precision and identification of machine- and sample-related systematic errors in monazite dating yields a chemical dating protocol that reproduces isotopic ages within error. The identification of systematic errors is very important to the chemical dating process, as such systematic errors may not always be obvious in the apparent age, due to compensatory cancellation. For example, the following three pairs of systematic

errors act to offset changes in the calculated age: 1) clipping of Th voltage pulse (-Th) and interference on lead background (-Pb); 2) non-correction of Ce Lα interference on Pb Mα for Ar detectors (+Pb) and misplacement of background collection position for U with respect to Ar Kα absorption edge (+U); 3) time-dependent lead spectrometer drift (-Pb) and monazite-quartz edge effect on ZAF correction (+Pb). Such systematic error pairs can change from additive to compensatory within a single grain as composition, position, and cumulative analysis time change.

Adoption of a maximum acceptable analytical precision places limits on the youngest ages determinable by chemical dating of monazite. Assuming an "average" metamorphic monazite composition of 2500 ppm U and 4 wt.% Th, and for the intrinsic detector response measured on the RPI JEOL 733 Superprobe, a cumulative analytical precision (e.g. $\sqrt{\varepsilon_U^2 + \varepsilon_{Th}^2 + \varepsilon_{Pb}^2}$) of 25% is obtained for a single 3-minute peak, 3-minute background analysis at a lead concentration of approximately 315 ppm. For the "average" metamorphic monazite given above, this yields a precision-limited minimum age of ~150 Ma. This minimum obtainable age is, of course, further a function of (U+Th) content and analytical time. An igneous monazite with 1 wt. % U, 10 wt. % Th, and the limiting Pb concentration of ~300 ppm yields, for the analytical conditions above, a precision limited age of ~50 Ma. If the cumulative analysis time is ~18 minutes (3 6-minute cycles), with 2500 ppm U and 4 wt. % Th, a cumulative analytical precision of 25 % is attained at ($315/\sqrt{3}$) ppm Pb, or ~180 ppm Pb. This combination of U, Th, and Pb concentrations yields a precision limited age estimate of $150/\sqrt{3}$ Ma, or ~85 Ma.

These observations are summarized in Figure 21, a plot of lead analytical precision (or, equivalently, lead concentration) vs. monazite age, for monazites with 1, 5, 10, 15, and 20 wt.% Th, respectively. For a 10-minute, 200 nA analysis, monazites with ≥ 1000 ppm Pb (Fig. 21a)

have an inherently high analytical precision (1σ RSD of 5% or less). If this precision (composition) is taken as limiting, this imposes a precision-limited age of 600 Ma for a monazite with 1% Th and 7500 ppm, and a precision-limited age of 90 Ma for a monazite with 20 wt. % Th and 7500 ppm U. However, tolerance of lower precisions (Fig. 21b) decreases the precision-limited age accordingly; adoption of a limiting Pb analytical precision of 20 % (1-σ RSD), or approximately 220 ppm Pb, yields precision-limited ages of ~ 140 Ma for a monazite with 1% Th and 7500 ppm, and ~20 Ma for a monazite with 20% Th and 7500 ppm U.

**CONCLUSION**

Chemical dating of monazite has been shown to be an extremely useful adjunct to traditional isotopic dating methods. Given the extreme variability in monazite composition, and the composition-dependent sensitivity of precision and accuracy of the chemical dating method, it is recognized that no one chemical dating protocol will optimize lead analytical precision. Instead, flexibility in parameters such as background collection position, beam diameter, analytical current, analysis time and, in some cases, analyzed lead line, is warranted. This paper has emphasized the role of detector gas in obtaining precise lead analyses, and the difficulties attached to analysis of lead with Ar detectors, but EMPs with Ar detectors can obtain lead analyses at the precision level of Xe detectors, provided special care is taken in modeling background and accounting for the presence of second-order LREE escape peaks.

Current and future EMP development emphasizes the incorporation of high-intensity diffraction crystals, improved stage movement resolution, and increased beam current at lower accelerating voltages. Such additions will improve analysis precision while reducing sample damage. However, rigorous evaluation of the accuracy of monazite chemical age determinations requires synthesis and complete chemical and crystallographic characterization of (U, Th, Pb)

bearing monazite age standards. Production of such a standard is the next step in improving this technique.

**ACKNOWLEDGEMENTS**

We thank Kiera Becker for maintenance of and assistance on the JEOL 733 Superprobe at RPI. Thanks also go to Mike Williams and Mike Jercinovic (University of Massachusetts Amherst) for organizing the Monazite Microprobe Geochronology short course at UMass in March of 2002, and to the above and Bob Tracy (Virginia Polytechnic Institute) for organizing the special session at the GSA 2002 annual meeting n Denver, CO. The free exchange of ideas and materials between our lab and the UMass lab has helped both groups in their attempts to tackle this important and intriguing analytical problem.

**REFERENCES**

Armstrong, J.T. (1984) Quantitative analysis of silicate and oxide minerals: a reevaluation of ZAF corrections and proposal for new Bence-Albee coefficients. Microbeam Analysis-1984, 19, 208-212.

Asami, M., Suzuki, K., and Grew, E.S. (2002) Chemical Th-U-total Pb dating by electron microprobe analysis of monazite, xenotime and zircon from the Archean Napier Complex, east Antarctica: evidence for ultra-high-temperature metamorphism at 2400 Ma. Precambrian Research, 114, 249-275.

Bastin, G.F., vanLoo, F.J.J., Heijligers, H.J.M. (1984) An evaluation of the use of Gaussian prz curves in quantitative electron probe microanalysis. X-Ray Spectrometry, 13, 91-97.

Bell, T.H. and Welch, P.W. (2002) Prolonged Acadian orogenesis: revelations from foliation intersection axis (FIA) controlled monazite dating of foliations in porphyroblasts and matrix. American Journal of Science, 302, 549-581.

Bevington, P.R. (1969) Data Reduction and Error Analysis for the Physical Sciences. McGraw-Hill, New York.

Boatner, L.A. (2002) Synthesis, structure, and properties of monazite, pretulite, and xenotime. Reviews in Mineralogy and Geochemistry, 48, 87-122.

Boatner, L.A., and Sales, B.C. (1988) Monazite. In: Radioactive Waste Forms for the Future (Luize, W. and Ewing, R.C., eds.). New York, Elsevier, 497-545.

Boggs, K.J.E., Kamo, S.L., Simony, P., Moore, J., and Archibald, D. (2002) A comparison of CHIME and ID-TIMS U-Pb monazite ages from the Rocky Mountain trench near Golden, British Columbia, Canada, and the importance of CHIME analyses. Geological Society of America, Abstracts with Programs, 34, 68 (Paper 25-7).

Catlos, E.J., Gilley, L.D., and Harrison, T.M. (2002) Interpretation of monazite ages obtained via in situ analysis. Chemical Geology, 188, 193-215.

Cherniak, D.J., Watson, E.B., Grove, M., and Harrison, T.M. (2003) Pb diffusion in monazite: a combined RBS/SIMS study. Chemical Geology, submitted.

Cho, K.-H., Takgaki, H., and Suzuki, K. (1999) CHIME monazite age of granitic rocks in the Sungchang shear zone, Korea; timing of dextral ductile shear. Geoscience Journal (Seoul), 3, 1-15.

Cocherie, A. and Albarede, F. (2001) An improved U-Th-Pb age calculation for electron microprobe dating of monazite. Geochimica et Cosmochimica Acta, 65, 4509-4522.

Daniel, C.G. and Pyle, J.M. (2002) Monazite thermochronometry in kyanite + sillimanite ± andalusite-bearing schists and from the Picuris Range, northern New Mexico. Geological Society of America, Abstracts with Programs, 34, 172 (Paper 76-3).

Donovan, J.J., Hanchar, J.M., Piccoli, P.M., Schrier, M.D., Boatner, L.A., and Jarosewich, E. (2003) A re-examination of the rare earth element orthophosphate reference samples for electron microprobe analysis. Canadian Mineralogist, submitted.

Duncumb, P. and Reed, S.J.B. (1968) The calculation of stopping power and backscattering effects in electron microprobe analysis. In Heinrich, K.F.J., (Ed) Quantitative Electron Microprobe Analysis, National Bureau of Standards Special Publication 298. U.S. Department of Commerce, Washington DC, 133-154.

Foster, G., Gibson, H.D., Parrish, R.R., Horstwood, M., Fraser, J., and Tindle, A. (2002) Textural, chemical, and isotopic insights into the nature and behaviour of metamorphic monazite. Chemical Geology, 191, 183-207.

Goldstein, J., Newbury, D., Echlin ,P., Joy, D., Fiori, D., and Lifshin, E. (1984) Scanning Electron Microscopy and X-Ray Microanalysis. Plenum, New York.

Grew, E.S., Suzuki, K., and Asami, M. (2001). CHIME ages of xenotime, monazite, and zircon from beryillum pegmatites in the Napier complex, Khmara Bay, Enderby Land, East Antarctica. Polar Geoscience, 14, 99-118.

Heinrich, K.F.J. (1985) A simple accurate absorption model Microbeam Analysis-1985, 20, 79-81.

Jenkins, R. and DeVries, J. (1982) Practical X-ray Spectrometry. Springer Verlag, Berlin.

Johann, H.H. (1931) Die Erzeugung lichstarker Röntgenspektren mit Hilfe von Konkavkristallen. Zeitschrift für Physik, 69,185-206.

Johannson, T. (1933) Über ein neuartiges genau fokussierendes Röntgenspektrometer. Zeitschrift für Physik, 82,507-528.

Karioris, F. G., Gowda, K.,and Cartz, L. (1991) Heavy ion bombardment on monoclinic $ThSiO_4$, $ThO_2$, and monazite. Radiation Effects Letters, 58, 1-3.

Kim, B.-C., Choi, S.-J., Suzuki, K., Adachi, M., Obayashi, T., and Yu, K.-M. (1997) Provenance of Cretaceous sandstones in the southeastern Youngdong Basin, Korea; CHIME geochronology of detrital monazites. Geoscience Journal (Seoul), 1, 37-49.

Krohe, A. and Wawrzenitz, N. (2000) Domainal variations of U-Pb monazite ages and Rb-Sr whole-rock dates in polymetamorphic paragneisses (KTB drill core, Germany): influence of strain and deformation mechanisms on isotope systems. Journal of Metamorphic Geology, 18, 271-291.

Meldrum, A., Boatner, L. A., and Ewing, R. C. (1997) Displacive radiation effects in the monazite- and zircon-structure orthophosphates. Physics Reviews B, 56, 13805-13814.

Montel, J.-M., Foret, S., Veschambre, M., Nicollet., and Provost, A. (1996). Electron microprobe dating of monazite. Chemical Geology, 131, 37-53.

Pan, Y. and Stauffer, M.R. (2000) cerium anomaly and Th/U fractionation in the 1.85 Ga Flin Flon paleosol: clues from REE- and U-rich accessory minerals and implications for paleoatmospheric reconstruction. American Mineralogist, 85, 898-911.

Parrish, R.R. (1990) U-Pb dating of monazite and its application to geological problems. Canadian Journal of Earth Sciences, 27, 1431-1450.

Pyle, J.M. (2001) Distribution of select trace elements in pelitic metamorphic rocks: pressure, temperature, mineral assemblage, and reaction-history controls. Ph.D. dissertation, Rensselaer Polytechnic Institute.

Pyle, J.M. and Spear, F.S. (2003) Four generations of accessory-phase growth in low-pressure migmatites from SW New Hampshire. American Mineralogist, 88, 338-351.

Pyle, J.M., Spear, F.S., and Wark, D.A. (2002). Electron microprobe analysis of REE in apatite, monazite, and xenotime: protocols and pitfalls. Reviews in Mineralogy and Geochemistry, 48, 337-362.

Reed, S.J.B. and Buckley, A. (1996) Virtual WDS. Mikrochimica Acta, 13, 479-483.

Roeder, P. (1985) Electron-microprobe analysis of minerals for rare-earth elements: use of calculated peak-overlap corrections. Canadian Mineralogist, 23, 263-271.

Scherrer, N.C., Engi, M., Gnos, E., Jakob, V., and Leichti, A. (2000) Monazite analysis; from sample preparation to microprobe age dating and REE quantification. Schweizerische Mineralogische und Petrographische Mitteilungen, 80, 93-105.

Scott, V.D., Love, G., and Reed, S.J.B. (1995) Quantitative Electron-Probe Microanalysis (second edition). Ellis Horwood Ltd, Chichester.

Sewell, D.A., Love, G., and Scott, V.D. (1985) Universal correction procedure for electron-probe microanalysis. I. Measurement of X-ray depth distributions in solids. Journal of Physics D, 18, 1233-1243.

Spear, F.S. and Pyle, J.M. (2002) Apatite, xenotime, and monazite in metamorphic rocks. Reviews in Mineralogy and Geochemistry, 48, 293-335.

Suzuki, K. and Adachi, M. (1991) Precambrian provenance and Silurian metamorphism of the Tsbonosawa paragneiss in the South Kitakami terrane, northeast Japan, as revealed by the chemical Th-U-total Pb isochron ages of monazite, zircon, and xenotime. Geochemical Journal, 25, 357-376.

Suzuki, K., Adachi, M., and Kajizuka, I. (1994) Electron microprobe observations of diffusion in metamorphosed detrital monazites. Earth and Planetary Science Letters, 128: 391-405.

Terry, M.P., Robinson, P., Hamilton, M.A., and Jercinovic, M.J. (2000) Monazite geochronology of UHP and HP metamorphism, deformation, and exhumation, Nordøyane, Western Gneiss Region, Norway. American Mineralogist, 85, 1651-1664.

Tomascak, P.B., Krogstad, E.J., and Walker, R.J. (1996) U-Pb monazite geochronology of granitic rocks from Maine: implications for late Paleozoic tectonics in the northern Appalachians. Journal of Geology, 104, 185-195.

Wendt, I. and Carl, C. (1991) The statistical distribution of the mean squared weighted deviation. Chemical Geology, 86, 1991.

Williams, M.L. and Jercinovic, M.J. (2002) Microprobe monazite geochronology: putting absolute time into microstructural analysis. Journal of Structural Geology, 24, 1013-1028.

Williams, M.L., Jercinovic, M.J., and Terry, M.P. (1999) Age mapping and dating of monazite on the electron mircroprobe: deconvoluting multi-stage histories. Geology, 27, 1023-1026.

**Appendix 1**: **Protocol for chemical age analysis of monazite. *indicates JEOL specific task**

Calibration standards given in Table 5, EMP hardware, calibration, and analysis settings listed in Table 7

1. Samples (standards) given 1-2 hour finishing colloidal silica CMP polish
2. Samples (standards) cleaned, dried at ~80°C for 2-12 hr,
3. Samples (standards) carbon coated to 200-300 Å thickness
4. Load samples Accelerating voltage set to 25 keV. *X-ray collimator slits set to open (3 mm) setting)
5. When vacuum reached desired level, saturate filament @ 25 keV
6. Set element background collection positions (Ce, Y, U, Th, Pb) to **calibration** positions. *Check for proper detector gain, bias, baseline, and voltage window settings.
7. Locate elemental peaks on standard for each element, and perform SCA scans on each peak at 10 nA and 250 nA to ensure no voltage clipping occurs for current detector settings.
8. Perform ≥ 3 calibrations for each element @ 10 nA on Faraday cup. Note large variations in initial k-ratio (k-ratio > 1.03 or k-ratio < 0.97) which may be caused by
   a. Carbon coat degradation
   b. Cleaning/repolishing of samples
   c. Faulty focus or filament saturation
   d. Change of or mis-aligment in X-ray collimators
   e. Previous mechanical servicing of EMP, or new EMP hardware

   Once desired number of successful calibrations are performed, average results of selected calibrations. Calibrate lead last.
9. Switch background collection positions to **analysis** positions.
10. Perform ≥ 5 measurements of Pb intensity on Pb standard (or, optionally, all measured elements on their respective standards) at analysis conditions (200 nA) to establish baseline for Pb calibration drift testing.
11. Perform ≥ 5 analyses of Y and Th standards to calculate average element interference correction factors for Th interference on U Mβ, and Th and Y interference on Pb Mα.
12. (Optional) Perform one SCA scan per element, at analysis conditions, for each separate monazite compositional domain previously identified in the sample, to ensure that voltage clipping is avoided.
13. Begin analysis of unknowns. Each single analytical cycle consists of simultaneous two-spectrometer measurement of Pb Ma for 3 minutes on peak, and 3 minutes total on high and low background, resulting in 6 total minutes of measurement of Pb Ma intensity per cycle., with lesser times for other elements (Table 9). Each spot should be analyzed for 2-5 cycles, or until beam damage renders the spot unusuable. Beam size should be on the order of 5-8 μm in diameter.
14. Repeat steps 10 and 11 every 1-2 hours, or as needed (depending on severity of observed drift). If drift is observed, restandardize.s
15. (Optional) Peform a final peak search and calibration (at calibration conditions – 10 nA) on Pb Mα.

16. If a significant deviation from the initial Pb k-ratio occurs during analysis (as shown by results of repeated (10,11)), regress Pb k-ratio against time so that a relation of the form

    $$\text{k-ratio}_{\text{Pb std}}(t) = mt + \text{k-ratio}_{\text{Pb std}}(t_0)$$

    is generated, where where m is the slope of the regression line relating time and Pb k-ratio, and $\text{k-ratio}_{\text{Pb std}}(t_0)$ is the initial Pb standard k-ratio. If the drift appears continuous, one regression line is calculated, and if the drift appears to have been punctuated, the regression line is divided into the appropriate number of segments. For the time *t* of each unknown point analysis, $\text{k-ratio}_{\text{Pb std}}(t)$ is calculated, the percentage change from the initial Pb standard k-ratio is calculated, and the unknown Pb k-ratio is multiplied by that factor. The drift corrected k-ratios are again *ZAF- or $\phi\rho z$-corrected.
17. If no drift of Pb calibration is apparent, correct for Th interference on U Mβ and Th + Y interference on Pb Mα by use of equations (5a, 5b, or 6), using correction factors measured on standards throughout the analytical session, and unknown k-ratios of Th and Y from individual unknown analyses.

For analysis of sample T22 performed on 13 February 2003, calibration information is given in Table 10. Three calibrations were performed on Y, Ce, and Th standards, U was calibrated 4 times, and Pb4 and Pb5 were calibrated 5 times. After initial measurement of Pb k-ratio at 200 nA (Fig. A1), correction factors were measured for Y and Th interference on Pb Mα (Table 10). During this analytical session, three blocks of unknown monazites were analyzed; T22 was the second of three blocks to be analyzed, and analysis required approximately 6 hours for 50 spot analyses. Five measurements of Pb standard k-ratio were made each on spectrometers 4 (Fig A1a) and 5 (Fig. A1b), immediately before and after the T22 analysis block, and these two k-ratio measurements formed part of a group of four measurements from which a linear correction for time-dependent spectrometer drift was generated:

$$\text{Pb4}_{\text{k-ratio,t}} = 0.0078(\text{time}) + 1.0103 \qquad \text{(A1-1a)}$$

$$\text{Pb5}_{\text{k-ratio,t}} = -0.1887(\text{time}) + 0.9995 \qquad \text{(A1-1b)}$$

After a fictive lead k-ratio at time t (analytical time) is calculated, the drift-corrected lead concentration is calculated as:

$$\text{Pb4}_{\text{corr,t}} = \text{Pb4}_{\text{uncorr,t}} * (\text{Pb4}_{\text{k-ratio,t}} / \text{Pb4}_{\text{k-ratio,t}_0}) \qquad \text{(A1-2a)}$$

$$\text{Pb5}_{\text{corr,t}} = \text{Pb5}_{\text{uncorr,t}} * (\text{Pb5}_{\text{k-ratio,t}} / \text{Pb5}_{\text{k-ratio,t}_0}) \qquad \text{(A1-2b)}$$

Where $\text{Pb4}_{\text{k-ratio,t}_0} = 1.0103$ and $\text{Pb5}_{\text{k-ratio,t}_0} = 0.9995$. For the drift correction factor measured in this analytical session, lead concentrations on spectrometer 4 increase less than 1 % over the analysis interval, but decrease 2-6 % on spectrometer 5 over the analysis interval.

Once drift-corrected lead concentrations are calculated, Pb concentrations are corrected, according to equation (6) for Th ($M\zeta_{1,2}$, M2-O4) and Y ($L\gamma_{2,3}$) interference, using the correction factors listed in Table 10, and U is corrected for Th ($M\gamma$) interference using equation 5a. Corrected U and Pb concentrations are inserted, along with Th concentration, into equation (1) (Montel et al., 1996), and equation (1) is solved iteratively for time, using the Microsoft Excel goal seek routine set to a maximum of 1000 iterations, with a tolerance of $1x10^{-8}$.

**Figure Captions**

**Figure 1**. VWDS scans (Reed and Buckley, 1996) centering on (a) U Mα, (b) U Mβ, (c), Pb Mα, and (d) Pb Mβ. Model scans generated with and accelerating voltage of 25 keV. Ar detector gas is used to induce second-order REE escape peaks. Critical monazite components are given in wt. % element.

**Figure 2**. (a) Ionization efficiency for Ar gas in the region of the Ar K absorption edge. Also shown for reference are the positions of nearby Th and U peaks. (b) WDS scan of a portion of the X-ray spectrum for Trebilcock (Tomascak et al., 1996) monazite, using a PET crystal and P10 detector gas at conditions given in the figure. The scan shows the presence of the Ar K absorption edge between the U Mβ and U Mα peaks, as well as the superior resolution of the U Mβ and its nearest neighbor (Th Mγ), relative to the adjacent U Mα – Th Mβ peaks. Peak-to-background ratios for background positions (a, b, c) are given in Table 2 and discussed in the text.

**Figure 3**. Wavelength dispersive scan of $PbSiO_3$ with PET crystal and Xe detector. Lead Mα and Mβ peaks are labeled. Scan conditions include accelerating voltage of 25 keV, absorbed current of 50 nA, 0.1 mm step size, and dwell time of 1 s per step.

**Figure 4**. (a) Statistical uncertainty in Pb counts for both uncorrected Pb Mα measurements and Pb Mα measurements corrected for Th and Y interference. Measurements (n=102) are on mid-Proterozoic (~1420 Ma) monazite from the Picuris Range, New Mexico, USA (Daniel and Pyle, 2002). Group in ellipse indicates high-Th monazite with significantly higher (worse) corrected lead analytical precision. (b) Comparison of counting errors associated with Pb Mα and Pb Mβ analysis for both Proterozoic and Paleozoic monazite. Diamonds = uncorrected Pb Mα counting errors; Squares = Pb Mα counting errors corrected for Th and Y interference. Counting error propagation associated with correction of element interferences discussed in text.

**Figure 5**. Effect of detector gas on wavelength-dispersive spectrum. (a) Virtual Pulse Height Analyzer (VPHA; Reed and Buckley, 1996) scan of Pb-bearing $CePO_4$, with spectrometer set to Pb Mβ position. A narrow voltage window filters out the second order Ce Lα peak, but the majority of the second order Ce escape peak falls within the voltage window set for passing the Pb Mβ peak. (b) VPHA scan of the same material, but using a Xe detector. The greater energy differential between the Xe absorption edge and the Ce La peak results in a Ce escape peak with a voltage distribution that falls outside of the voltage window. (c) Wavelength dispersive spectrum of Pb-doped $CePO_4$ generated with both Ar and Xe detectors. The distribution and diminished voltage intensity of the second order Ce escape peaks (and second order REE peaks, in general) results in the disappearance or diminishment of the second order Ce peaks in the WD spectrum.

**Figure 6**. WDS scans of Trebilcock monazite using a PET crystal (190-140 mm) and simultaneous acquisition on both Ar and Xe detectors at variable X-ray collimator settings of (a) 3mm, (b) 500 μm), and (c) 300 μm. The dotted line in each scan gives absorbed current as a function of spectrometer position; duration of each scan required approximately 24 minutes. Background counts at Pb Mα, Ce Lα (n=2), and Pb Mβ are calculated by fitting an exponential function regression to the background regions (black line segments) indicated on each spectrum. All REE peaks visible on these spectra are second-order escape peaks resulting form interaction of REE X-rays with Ar detector gas.

**Figure 7** Plots of Pb Mα and Pb Mβ (a) peak intensity (counts/second) and (b) peak-to-background ratio, Trebilcock monazite, vs. X-ray collimator width, for slit widths of 3 mm, 500 μm, and 300 μm. Data for these figures taken from Figure 6. Solid symbols = argon detectors. Open symbols = xenon detectors.

**Figure 8**. Assessment of background position placement in monazite analyses. (a) Scan of Trebilcock monazite with Ar detector gas. (b) Scan of Trebilcock monazite with Xe detector gas. Characteristic peaks are labeled in (a) – all visible REE peaks are second-order escape peaks. Eyeball background fits are indicated by grey curves, and the position of the Ar detector background line is indicated by the upper of the two grey curves in (b). Preferred background collection positions for both Pb Mα and Pb Mβ are indicated in (a) and (b). Note the difference in the vertical scales between (a) and (b). An X-ray collimator width of 500 μm was used for both scans.

**Figure 9**. Plot of Pb counting error vs. time. An intrinsic detector response of 0.33 counts Pb/sec•nA•wt.% Pb was measured at 200 nA on Trebilcock monazite, and used to construct this figure. a) Plot of Pb 1-sigma counting error vs. time for material with 10000 ppm Pb (bottom line), 1500 ppm Pb (middle line) and 250 ppm Pb (top line). Boxed area in (a) is expanded in (b), showing detail of counting precision with changing time, up to a maximum of 50 minutes. One-sigma counting errors at 10 minutes are 11.7 % (point A), 2.1 % (point B), and 0.5 % (point C) for 250 ppm Pb, 1500 ppm Pb, and 10000 ppm Pb, respectively. The quoted counting errors translate to 2-sigma compositional uncertainties shown in (b).

**Figure 10**. Comparison of observed and predicted lead concentration in Trebilcock monazite for groupings of (a) 10 measurements and (b) 90 measurements. All measurements on Pb Mβ with a Xe detector. Error bar = ± 1 standard error of the mean.

**Figure 11**. Summary plot of monazite U-Th-total Pb chemical ages, LM samples. (a) histogram of monazite chemical age distributions. Bin width equals 10 My. (b) Probability distribution plot of LM monazite chemical ages. Grey peaks show Gaussian distribution about mean age of each compositional domain, for associated standard error of the mean. Number of analyses per domain indicated in parentheses. Black line shows sum of individual probability distribution plots. From Pyle et al. (this volume)

**Figure 12**. image of pre- and post- colloidal silica polishing. a) Reflected light photomicrograph of monazite inclusion in garnet, sample T22, with surface pitting and plucked grain boundaries. Large dark spots are ion-beam pits. Polish shown is 1 μm diamond paste finish. b) same grain after 4-hour treatment with colloidal silica chemical-mechanical polishing. Note that majority of plucked monazite grain boundaries have been brought out by polishing to reveal grain-boundary alteration assemblage. c) Enlargement of left-side monazite grain boundary, showing detail of alteration assemblage, which consists of a mixture of apatite, quartz, and Fe-Ti-oxide.

**Figure 13**. Single-channel analyzer (SCA) scans of $CePO_4$ doped with Pb, with spectrometer at Ce Lα (n=1) position (a) SCA scan at low count-rate condition; voltage window optimized to include counts due to only Ce La x-rays. (b) SCA scan at high count-rate condition; increased count rate results in pulse shift to lower voltages (Goldstein et al., 1984), with result that detector baseline and window settings now exclude approximately 10 % of total Ce Lα X-ray intensity.

**Figure 14**. (a) Plot of change in diffraction crystal two-theta angle as a function of temperature (Jenkins and DeVries, 1982). Diffraction crystals shown are LiF, ADP, and PET. PET is particularly sensitive to temperature changes. Pb Mα measured on PET has a two-theta angle of 35.2°. A change in ambient temperature of 5°C results in a Pb Mα $\Delta 2\Theta$ of 0.025°, which translates to a loss of approximately 20 % of lead Mα counts, as measured on the JEOL 733.(b) Plot of k-ratio vs. time for measurements of Pb Mα k-ratio on lead standard $PbSiO_3$. Duration of experiment approximately 3 1/4 hours. Error bars are ± 2σ. Over span of measurements, Pb k-ratio has decreased by approximately 2 %, implying that lead measurements in unknown taken at the end of this time span are 2 % lower than measurements of the same spot taken just after calibration.

**Figure 15**. Uncertainties associated with selection of various ZAF correction models. (a) Uncertainty in Pb concentration. (b) Uncertainty in age. ZAF correction models are those of Armstrong (1984), Heinrich (1985), Sewell et al. (1985), Bastin et al. (1984), and Duncumb and Reed (1968). Error bars in both graphs are ±2σ

**Figure 16**. Grain damage from chemical age analysis of monazite. Both grains (a) and (b) are from the same thin section, and were analyzed at identical conditions including ~200 nA cup current, 25 keV accelerating voltage, 6-8 μm beam diameter, and and approximately 30 minutes of continuous analytical time per spot (5 spots at 6 minutes each). In (a), the monazite surface shows slight spotting, whereas ib (b), a sizeable crater approximately 6-8 mm across has been formed at the site of each analysis. A crack runs across the monazite grain just below the lower spot in grain (b), and the sample has the appearance of having undergone melting, which may be related to a number of factors including composition, subsurface inclusion density, beam arcing, or the presence of adsorbed fluids on the grain surface. (c) plot of Y concentration, corrected Pb concentration, and correction for Y interference on Pb, for a 5-cycle, same-spot analysis (35 minute beam exposure), and a 4-cycle, same-spot analysis (28 minute beam exposure). Yttrium concentration (squares) given on left y axis, and concentration of measured lead (solid circles) and apparent lead due to yttrium interference (open circles) given on right y axis. Italic numbers below symbol for yttrium concentration indicate absorbed current at start of analysis. Error bars are 1-sigma; size of yttrium error bars equal to or smaller than plotted symbol.

**Figure 17**. Schematic of emergent X-rays produced during monazite analysis. Two X-ray production volumes are indicated by tear-drop shaped cross-sections. X-rays from excitation volume 1 are collected by spectrometers A1 and B1, and X-rays from excitation volume 2 are collected by spectrometers A2 and B2 X-rays collected by different spectrometers may sample X-rays that have passed through areas of highly different composition (zonal domains) or atomic number and/or absorption potential (adjacent grains or micro-inclusions), resulting significantly different calculated lead concentrations.

**Figure 18**. BSE images of Trebilcock monazite depicting a series of traverses (a,b,c), each with a different grain orientation, to investigate possible relationships between grain/spectrometer orientation, edge effects/spectrometer orientation, and calculated compositions. Approximate orientation of the five spectrometers shown on each panel. Direction of traverse indicated by arrow – numbers on traverse line relate to line plot shown in Figure 19.

**Figure 19**. Line plot of Pb k-ratio for individual point analyses, Trebilcock monazite. Number above traverses 1-8 correlated with traverse lines 1-8 on Figure 20. Step size in each traverse is approximately 2 μm, and Pb k-ratios are collected simultaneously on spectrometers 2 (diamonds), 3 (squares), 4 (triangles), and 5 (circles). Note that k-ratio may increase or decrease at monazite-epoxy boundary, depending on orientation of spectrometer relative to grain edge and traverse orientation.

**Figure 20**. (a) Back-scatter electron image of monazite inclusion in garnet, sample T22. (b) image from (a) with analysis positions labeled. Size of analytical label is approximately twice the beam diameter used in analysis. (c) Age histogram for analyses shown in (c). Bin width equals 15 m.y. Curve is a gaussian approximation to age distribution, with average age of 418 Ma, and standard deviation, based on grouped average of ages, of 41 Ma. (d) Histogram comparing age distribution for monazite, sample T22, from chemical analyses (gray) and isotopic analyses (hachured). Cumulative frequency of isotope analysis age bins normalized to 50 total analyses, to match number of chemical age determinations.

**Figure 21**. Plot of lead precision and concentration vs age for intrinsic detector response (Xe, with PET, spectrometer #4) measured on the JEOL 733 Superprobe at RPI. Analytical time is fixed at 10 minutes (600 sec) ,with analysis current of 200 nA. (a) Plot for lead analytical standard deviations of 0-20 %. (b) Plot for lead analytical standard deviations of 10-40 %. Both plots incorporate a fixed U concentration of 7500 ppm. Curves are plotted for monazites with Th concentrations of 1, 5, 10, 15, and 20 wt. %.

**Figure A1**. Corrections for drift (a) PET, spectrometer 4. (b) PET, spectrometer 5. Each point is an average of five lead k-ratio measurements on $PbSiO_3$. Both spectrometers experienced non-linear drift, which is modeled by dividing the overall analytical session into 2 segments. In each segment, drift is modeled as a linear function of time. Analysis segment 1 is indicated by black squares, and analysis segment 2 is indicated by grey triangles. T22 was analyzed during segment 1, over the time interval indicated by the grey bar on the x-axis of both (a) and (b), and the drift correction equations applied to lead measurement in T22 are italicized. Note that the mechanism responsible for drift causes an increase in k-ratio for spectrometer 4, but a decrease in k-ratio for spectrometer 5.

**Table 1**. Average pelite monazite composition (Pyle, 2001) for use in ZAF correction

| oxide | Oxide wt % | 1-sigma | Element wt% | +2-sigma El | -2 sigma El |
|---|---|---|---|---|---|
| $SiO_2$ | 0.23 | 0.21 | 0.11 | 0.30 | < 0 |
| $P_2O_5$ | 29.87 | 0.72 | 13.03 | 13.66 | 12.40 |
| CaO | 0.90 | 0.25 | 0.65 | 1.00 | 0.29 |
| $La_2O_3$ | 14.07 | 0.80 | 12.00 | 13.36 | 10.63 |
| $Ce_2O_3$ | 29.54 | 1.33 | 25.22 | 27.49 | 22.95 |
| $Pr_2O_3$ | 2.92 | 0.19 | 2.50 | 2.82 | 2.17 |
| $Nd_2O_3$ | 12.41 | 0.7 | 10.64 | 11.84 | 9.44 |
| Sm2O3 | 1.89 | 0.3 | 1.63 | 2.15 | 1.11 |
| $Gd_2O_3$ | 1.56 | 0.35 | 1.35 | 1.96 | 0.75 |
| $Dy_2O_3$ | 0.59 | 0.28 | 0.51 | 1.00 | 0.03 |

Average of 526 analyses. Elements measured in monazite chemical age analysis include Y, Ce, Pb, U, Th. Ce was not measured in an earlier analytical protocol.

**Table 2**. Peak counts with respect to Ar K absorption edge (123.98 on PET) (Fig. 2)

U Mβ - ages on Trebilcock monazite, with U corrections to bk b and bk c

| | Position (mm) | counts | Bkgrd cts under peak | P-B | (P-B)/B | Δ (%) | ppm U | Age M.y. |
|---|---|---|---|---|---|---|---|---|
| pk | 119.0 | 1428 | | | | | | |
| low bk | 115.0 | 952 | | | | | | |
| hi bk a | 121.5 | 748 | 826 (1) | 826 | 0.73 | | 5465 | 280 |
| hi bk b | 124.4 | 316 | 681 (2) | 681 | 1.10 | 50.6 | 8230 | 262 |
| hi bk c | 128.1 | 270 | 744 (3) | 744 | 0.92 | 26.4 | 6908 | 270 |

**Table 3**. P/B ratios, Trebilcock monazite, for various X-ray collimator settings (Figure 6)

| Slit size | spec | Pb Mα | | | | Pb Mβ | | | | Ce Lα | | | | time (sec) |
|---|---|---|---|---|---|---|---|---|---|---|---|---|---|---|
| | | P | B | P/B | 1-σ (%) | P | B | P/B | 1-σ (%) | P | B | P/B | 1-σ (%) | |
| 300 μm | | | | | | | | | | | | | | |
| | 3 (Ar) | 209 | 128 | 1.64 | 22.52 | 212 | 164 | 1.30 | 40.13 | 358 | 154 | 2.32 | 11.11 | 5 |
| | 4 (Xe) | 204 | 107 | 1.90 | 18.29 | 215 | 81 | 1.60 | 23.13 | 161 | 128 | 1.26 | 51.86 | 5 |
| Background range: high 180-175 mm; low 149.8-147.2 mm | | | | | | | | | | | | | | |
| 500 μm | | | | | | | | | | | | | | |
| | 3 (Ar) | 354 | 216 | 1.64 | 17.29 | 362 | 264 | 1.37 | 25.46 | 677 | 253 | 2.68 | 7.19 | 5 |
| | 4 (Xe) | 208 | 115 | 1.64 | 19.56 | 198 | 144 | 1.37 | 34.32 | 145 | 138 | 1.05 | 227.91 | 5 |
| Background range: high 178-175 mm; low 161.2-159.8 mm | | | | | | | | | | | | | | |
| 3 mm | | | | | | | | | | | | | | |
| | 3 (Ar) | 528 | 344 | 1.54 | 16.01 | 786 | 413 | 1.90 | 9.27 | 1173 | 397 | 2.96 | 5.10 | 5 |
| | 4 (Xe) | 350 | 210 | 1.67 | 16.89 | 369 | 260 | 1.42 | 22.97 | 292 | 249 | 1.17 | 53.66 | 5 |
| Background range: high 180-175 mm; low 161.4-156.4 mm | | | | | | | | | | | | | | |

**Table 4** Magnitude of correction for interference, and effect on age

| sample | Analy # | Raw Th | Raw Y | Raw U | Raw Pb | Raw age | Corr U | Corr Pb | Corr age | Δ% |
|---|---|---|---|---|---|---|---|---|---|---|
| 94-27 low Th | 98 | 37300 | 10549 | 15153 | 5938 | 1421 | 15042 | 5848 | 1408 | 0.91 |
| 00-2A hi Th/U | 12 | 97800 | 10728 | 21779 | 11136 | 1389 | 21487 | 10968 | 1377 | 0.86 |
| 00-2A low Th | 19 | 23028 | 8547 | 4007 | 2487 | 1452 | 3939 | 2423 | 1426 | 1.79 |
| BF-64 hi Th | 3a | 108800 | 13714 | 5975 | 2453 | 427 | 5570 | 2167 | 382 | 10.5 |
| BF–64 low Th | 5 | 32700 | 3956 | 3312 | 720 | 371 | 3191 | 636 | 331 | 10.8 |
| TM-637 | 4 | 24100 | 10729 | 5158 | 725 | 397 | 5069 | 631 | 349 | 12.9 |
| Trebilcock | 3 | 112800 | 19339 | 5726 | 1844 | 314 | 4929 | 1534 | 267 | 14.96 |

Units of concentration are ppm; units of age are M.y.

**Table 5**. Standards used in monazite chemical dating

| Element | standard | nominal elemental composition (wt %) | Standard: unknown ratio | Synthesis method |
|---|---|---|---|---|
| Y | $YPO_4$ | 48.35 % Y, 16.84 % P, 34.80 % O | 10-100 | REE(OH)gel, 1 atm non-Pb flux growth |
| Ce | $CePO_4$ | 59.60 % Ce, 13.18 % P, 27.22 % O | 2-3 | REE(OH)gel, 1 atm non-Pb flux growth, REE(OH)gel, 10 kb piston-cylinder |
| Pb | $PbSiO_3$ | 73.14 % Pb, 9.91 % Si, 16.94 % O | 50-5000 | Pb, Si oxides, 1 atm melt/xtln |
| Th | $ThSiO_4$ | 71.59 % Th, 8.67 % Si, 19.74 % O | 3-30 | REE(OH)gel, 1 atm non-Pb flux growth |
| U | $UO_2$ | 88.15 % U, 11.85 % O | 30-500 | REE(OH)gel, 1 atm non-Pb flux growth |

**Table 6**. Value range, counts per second, for measured elements in monazite chemical age analysis

| Element & Line | gas | xtl | calibration, cps | correction factor, cps | analysis, cps |
|---|---|---|---|---|---|
| Pb Mα | Xe | PET | 400-550 | --------- | 0-150 |
| Pb Mβ | Xe | PET | 350-550 | --------- | 0-100 |
| U Mβ | Ar | PET | 600-1800 | --------- | (0)(10)25-1050 |
| Th Mα | Ar | PET | 250-800 | ~15000 | (0)150-3500 |
| Y Lα | Ar | TAP | 4000-5000 | ~90000 | 500-3500 |
| Ce Lα | Ar | PET | ~2500 | --------- | 8500-25000 |

**Table 7**. EMP settings for monazite chemical age calibration and analysis

Part I: calibration

| Element (spec) | crystal | gas | peak | Gain (V) | Bias (V) | Baseline (V) | Window (V) | high bkg (+mm) | low bkg (-mm) | Max Peak time (s) | Max total Background time (s) |
|---|---|---|---|---|---|---|---|---|---|---|---|
| Y (1) | TAP | Ar | Lα | 12 | 1693 | 11 | 50 | 1.20 | 1.60 | 100 | 100 |
| Ce (2) | PET | Ar | Lα | 7 | 1680 | 23 | 58 | 4.00 | 3.00 | 10 | 10 |
| Pb4 (4) | PET | Xe | Mα | 20 | 1810 | 20 | 35 | 6.27 | 12.73 | 180 | 180 |
| Pb5 (5) | PET | Xe | Mα | 20 | 1810 | 15 | 35 | 6.27 | 12.73 | 180 | 180 |
| Th (3) | PET | Ar | Mα | 7 | 1725 | 15 | 35 | 4.00 | 4.00 | 80 | 80 |
| U (3) | PET | Ar | Mβ | 6 | 1735 | 15 | 45 | 4.00 | 3.00 | 80 | 80 |

Part II: analysis

| Element (spec) | crystal | gas | peak | Gain (V) | Bias (V) | Baseline (V) | Window (V) | high bkg (+mm) | low bkg (-mm) | Max Peak time (s) | Max total Background time (s) |
|---|---|---|---|---|---|---|---|---|---|---|---|
| Y (1) | TAP | Ar | Lα | 12 | 1693 | 11 | 50 | 1.20 | 1.60 | 100 | 100 |
| Ce (2) | PET | Ar | Lα | 7 | 1680 | 23 | 58 | 1.50 | 1.50 | 10 | 10 |
| Pb4 (4) | PET | Xe | Mα | 20 | 1810 | 20 | 35 | 6.27 | 3.90 | 180 | 180 |
| Pb5 (5) | PET | Xe | Mα | 20 | 1810 | 15 | 35 | 6.27 | 3.90 | 180 | 180 |
| Th (3) | PET | Ar | Mα | 7 | 1725 | 15 | 35 | 2.70 | 3.00 | 80 | 80 |
| U (3) | PET | Ar | Mβ | 6 | 1735 | 15 | 45 | 2.50 | 3.00 | 80 | 80 |

spec: spectrometer number
Pb4: lead measured on spectrometer 4
Pb5: lead measured on spectrometer 5

Detector settings are specific to the JEOL 733 Superprobe EMP at Rensselaer Polytechnic Institute. Background offsets are for a 140 mm Rowland circle.

**Table 8**. Possible sources of inaccuracy in monazite chemical dating

| Quantifiable sources | Magnitude of error | Non-quantifiable sources |
|---|---|---|
| Dead time | 1-2% (i) | Sample damage (?) |
| Peak drift | 1-10% (d) | Small scale sample heterogeneity (?) |
| Voltage pulse shift | 1-10% (i) | Edge effect; variable Z and A (i) |
| ZAF correction model | 1-2% (?) | |

most common effect on calculated age indicated by letter/symbol in parentheses:
i: increase calculated age
d: decrease calculated age
?: generally indeterminate

**Table 9**. Effect of ZAF corrections on chemical age (Figure 15)

Part I: model selection

| element | Th | U | Pb | Σ | | |
|---|---|---|---|---|---|---|
| Comp 1 sigma (%) | 0.83 | 1.58 | 5.15 | 5.45 | | |
| k-ratio | 0.1378 | 0.005487 | 0.001679 | | | |
| ZAF model | wt% Th | wt % U | wt % Pb | ±2 sigma wt % Pb | Age Ma | ±2 sigma age (10.9%) |
| Armstrong | 11.46 | 0.5303 | 0.1671 | ±0.0172 | 284 | ±31 |
| Heinrich | 11.63 | 0.5350 | 0.1668 | ±0.0172 | 280 | ±31 |
| Love/Scott I | 11.65 | 0.5503 | 0.1697 | ±0.0175 | 283 | ±31 |
| Bastin | 11.51 | 0.5677 | 0.1696 | ±0.0175 | 285 | ±31 |
| Duncumb/Reed | 11.75 | 0.5989 | 0.1651 | ±0.0170 | 270 | ±29 |

Part II: variation in value of fixed element concentration. ZAF model used is Heinrich (1985)

| | O | P | La | Ce | Pr | Nd | Sm | Gd | Y | U | Pb | Th | Age (Ma) |
|---|---|---|---|---|---|---|---|---|---|---|---|---|---|
| Std | 26.66 | 13.03 | 12.00 | 25.20 | 2.50 | 10.60 | 1.63 | 1.35 | 1.2596 | 0.5406 | 0.1526 | 10.71 | 275 |
| O=30 | **30.00** | 13.03 | 12.00 | 25.20 | 2.50 | 10.60 | 1.63 | 1.35 | 1.2595 | 0.5425 | 0.1526 | 10.74 | 274 |
| P=15 | 26.66 | **15.00** | 12.00 | 25.20 | 2.50 | 10.60 | 1.63 | 1.35 | 1.2541 | 0.5426 | 0.1535 | 10.75 | 275 |
| La=15 | 26.66 | 13.03 | **15.00** | 25.20 | 2.50 | 10.60 | 1.63 | 1.35 | 1.2612 | 0.5390 | 0.1523 | 10.68 | 275 |
| Ce=30 | 26.66 | 13.03 | 12.00 | **30.00** | 2.50 | 10.60 | 1.63 | 1.35 | 1.2647 | 0.5386 | 0.1523 | 10.67 | 275 |
| Pr=6 | 26.66 | 13.03 | 12.00 | 25.20 | **6.00** | 10.60 | 1.63 | 1.35 | 1.2644 | 0.5395 | 0.1525 | 10.69 | 275 |
| Nd=15 | 26.66 | 13.03 | 12.00 | 25.20 | 2.50 | **15.00** | 1.63 | 1.35 | 1.2668 | 0.5394 | 0.1526 | 10.69 | 275 |
| Sm=5 | 26.66 | 13.03 | 12.00 | 25.20 | 2.50 | 10.60 | **5.00** | 1.35 | 1.2691 | 0.5400 | 0.1529 | 10.70 | 275 |
| Gd=5 | 26.66 | 13.03 | 12.00 | 25.20 | 2.50 | 10.60 | 1.63 | **5.00** | 1.2677 | 0.5403 | 0.1528 | 10.71 | 275 |

Bold indicates varied element

**Table 10**: Chemical age analyses of monazite from Cavendish formation, Star Hill, Vermont, USA
Calibration and correction information

| date | el | # cal | C/nA•s | sec | nA (cup) | 1-σ (%) | CF Pb interference | CF U interference |
|---|---|---|---|---|---|---|---|---|
| 2/03 | Y | 3 | 503.2 | 30 | 10.03 | 0.29 | 0.003749±0.000166 Pb4 (3), 0.003466±0.000077 Pb5 (3) | ------- |
| 2/03 | Ce | 3 | 267.5 | 30 | 10.02 | 0.37 | ------- | ------- |
| 2/03 | U | 4 | 187.0 | 30 | 10.03 | 0.43 | ------- | ------- |
| 2/03 | Th | 3 | 83.8 | 30 | 10.03 | 0.64 | 0.001738±0.000062 Pb4 (3), 0.001469±0.000043 Pb5 (3) | 0.002806 (3) |
| 2/03 | Pb4 | 5 | 58.3 | 30 | 10.03 | 0.76 | ------- | ------- |
| 2/03 | Pb5 | 5 | 49.8 | 30 | 10.03 | 0.82 | ------- | ------- |

Analysis info T22 mnz 1 (analyzed 2/14/2003 (Pb Mα analysis)

| spot number (domain) | Th | Y | U* | Pb4* | Pb5* | 1-σ U (%) | 1-σ Th (%) | 1-σ Pb4 (%) | 1-σ Pb5 (%) | age 4 (Ma) | 1-s (Ma) | age 5 (Ma) | 1-s (Ma) | grouped age (Ma) | 1-s (Ma) |
|---|---|---|---|---|---|---|---|---|---|---|---|---|---|---|---|
| 1 (c) | 2.20 | bdl | 4247 | 750 | 673 | 2.38 | 0.98 | 9.42 | 10.39 | 438 | 43 | 419 | 45 | 429 | 13 |
| 2 (c) | 2.24 | bdl | 3589 | 709 | 528 | 2.82 | 0.98 | 10.10 | 13.30 | 433 | 46 | 347 | 47 | 390 | 61 |
| 3 (c) | 2.06 | bdl | 3580 | 659 | 552 | 2.81 | 1.02 | 10.76 | 12.85 | 426 | 48 | 383 | 51 | 405 | 30 |
| 4 (c) | 2.04 | bdl | 2936 | 574 | 484 | 3.38 | 1.02 | 12.25 | 14.56 | 397 | 51 | 362 | 54 | 379 | 25 |
| 5 (r) | 5.78 | bdl | 3555 | 1381 | 1224 | 2.73 | 0.82 | 5.43 | 5.94 | 405 | 25 | 394 | 26 | 400 | 8 |
| 6 (r) | 5.68 | bdl | 14581 | 2278 | 2010 | 0.91 | 0.82 | 3.36 | 3.86 | 461 | 16 | 431 | 17 | 446 | 22 |
| 7 (r) | 5.39 | bdl | 2074 | 1323 | 1141 | 4.43 | 0.81 | 5.54 | 6.30 | 444 | 32 | 420 | 33 | 432 | 17 |
| 8 (r) | 7.44 | bdl | 2137 | 1681 | 1569 | 4.24 | 0.82 | 4.44 | 4.66 | 418 | 26 | 430 | 27 | 424 | 9 |
| 9 (r) | 5.59 | bdl | 2063 | 1386 | 1137 | 4.49 | 0.81 | 5.27 | 6.34 | 451 | 31 | 405 | 32 | 428 | 32 |
| 10 (r) | 6.55 | bdl | 2151 | 1331 | 1322 | 4.26 | 0.82 | 5.52 | 5.55 | 367 | 26 | 407 | 29 | 387 | 28 |
| 11 (c) | 2.35 | bdl | 4082 | 699 | 716 | 2.50 | 0.96 | 10.26 | 10.05 | 395 | 42 | 434 | 45 | 414 | 28 |
| 12 (c) | 2.24 | bdl | 3443 | 870 | 617 | 0.98 | 2.93 | 8.16 | 11.61 | 544 | 47 | 411 | 49 | 477 | 94 |
| 13 (r) | 5.50 | bdl | 1665 | 1157 | 968 | 5.36 | 0.81 | 6.24 | 7.21 | 385 | 32 | 358 | 32 | 371 | 19 |
| 14 (c) | 2.39 | bdl | 3918 | 740 | 648 | 2.61 | 0.96 | 9.59 | 10.98 | 420 | 42 | 395 | 45 | 408 | 17 |
| 15 (c) | 2.56 | bdl | 4076 | 755 | 736 | 2.52 | 0.93 | 9.48 | 9.82 | 403 | 40 | 423 | 43 | 413 | 14 |
| 16 (c) | 3.39 | bdl | 4361 | 948 | 715 | 2.35 | 0.85 | 7.67 | 10.02 | 407 | 33 | 334 | 34 | 370 | 52 |
| 17 (c) | 3.43 | bdl | 4150 | 930 | 895 | 2.47 | 0.84 | 7.76 | 8.13 | 401 | 33 | 418 | 36 | 409 | 12 |
| 18 (c) | 3.07 | bdl | 3825 | 924 | 884 | 2.65 | 0.87 | 7.72 | 8.19 | 444 | 36 | 457 | 40 | 451 | 9 |
| 19 (r) | 5.91 | bdl | 9026 | 1716 | 1701 | 1.28 | 0.82 | 4.39 | 4.49 | 402 | 19 | 429 | 20 | 416 | 19 |
| 20 (c) | 2.45 | bdl | 3757 | 763 | 666 | 2.69 | 0.95 | 9.31 | 10.81 | 432 | 42 | 405 | 45 | 419 | 19 |
| 21 (c) | 2.26 | bdl | 3793 | 778 | 589 | 2.68 | 0.98 | 9.17 | 12.19 | 466 | 45 | 378 | 47 | 422 | 63 |
| 22 (c) | 2.17 | bdl | 3590 | 736 | 651 | 2.83 | 1.00 | 9.74 | 11.21 | 461 | 47 | 435 | 50 | 448 | 18 |
| 23 (r) | 6.78 | 6651 | 5701 | 1688 | 1468 | 1.86 | 0.82 | 4.49 | 5.05 | 392 | 19 | 380 | 21 | 386 | 8 |
| 24 (r) | 7.04 | bdl | 9809 | 2142 | 2027 | 1.20 | 0.82 | 3.63 | 3.87 | 435 | 17 | 442 | 18 | 438 | 5 |

**Table 10** (cont)

| spot number (domain) | Th | Y | U* | Pb4* | Pb5* | 1-σ U (%) | 1-σ Th (%) | 1-σ Pb4 (%) | 1-σ Pb5 (%) | age 4 (Ma) | 1-s (Ma) | age 5 (Ma) | 1-s (Ma) | grouped age (Ma) | 1-s (Ma) |
|---|---|---|---|---|---|---|---|---|---|---|---|---|---|---|---|
| 25 (r) | 6.90 | bdl | 9863 | 1935 | 1892 | 1.20 | 0.82 | 3.69 | 4.12 | 427 | 17 | 418 | 18 | 423 | 7 |
| 26 (r) | 6.86 | bdl | 10232 | 2018 | 1871 | 1.16 | 0.82 | 3.57 | 4.17 | 442 | 17 | 410 | 18 | 426 | 22 |
| 27 (r) | 6.88 | bdl | 9530 | 1889 | 2050 | 1.22 | 0.82 | 3.79 | 3.84 | 423 | 17 | 458 | 19 | 440 | 25 |
| 28 (r) | 7.00 | bdl | 6549 | 1612 | 1585 | 1.64 | 0.82 | 4.33 | 4.79 | 395 | 19 | 388 | 20 | 391 | 5 |
| 29 (r) | 7.03 | bdl | 10244 | 1998 | 1951 | 1.16 | 0.82 | 3.60 | 4.01 | 430 | 17 | 421 | 18 | 426 | 7 |
| 30 (r) | 5.46 | bdl | 15060 | 2052 | 2003 | 0.90 | 0.81 | 3.55 | 3.99 | 442 | 17 | 432 | 18 | 437 | 7 |
| 31 (r) | 4.00 | 3026 | 1043 | 716 | 808 | 8.41 | 0.81 | 8.76 | 8.75 | 369 | 45 | 416 | 51 | 392 | 33 |
| 32 (r) | 7.18 | bdl | 9322 | 1987 | 1945 | 1.24 | 0.82 | 3.61 | 4.02 | 434 | 17 | 425 | 18 | 430 | 6 |
| 33 (c) | 2.59 | bdl | 3902 | 676 | 758 | 2.62 | 0.93 | 9.82 | 9.71 | 392 | 40 | 438 | 44 | 415 | 33 |
| 34 (r) | 5.72 | bdl | 17447 | 2165 | 2294 | 0.82 | 0.82 | 3.36 | 3.51 | 424 | 15 | 449 | 17 | 437 | 17 |
| 35 (c) | 3.08 | bdl | 4427 | 924 | 925 | 2.34 | 0.87 | 7.33 | 8.04 | 456 | 35 | 456 | 38 | 456 | 0 |
| 36 (c) | 2.32 | bdl | 3580 | 629 | 544 | 2.83 | 0.97 | 10.54 | 13.44 | 404 | 44 | 350 | 48 | 377 | 38 |
| 37 (c) | 2.47 | bdl | 3790 | 646 | 663 | 2.70 | 0.95 | 10.27 | 11.04 | 390 | 42 | 400 | 46 | 395 | 7 |
| 38 (c) | 2.43 | bdl | 3476 | 640 | 652 | 2.92 | 0.95 | 10.43 | 11.34 | 402 | 44 | 409 | 48 | 405 | 5 |
| 39 (c) | 2.77 | bdl | 4018 | 724 | 646 | 2.55 | 0.91 | 9.09 | 11.20 | 397 | 38 | 355 | 41 | 376 | 30 |
| 40 (c) | 2.50 | bdl | 3709 | 676 | 781 | 2.75 | 0.94 | 9.83 | 9.45 | 407 | 42 | 469 | 46 | 438 | 44 |
| 41 (c) | 2.36 | bdl | 3796 | 745 | 724 | 2.69 | 0.97 | 9.00 | 10.13 | 462 | 44 | 450 | 47 | 456 | 9 |
| 42 (c) | 2.46 | bdl | 3900 | 744 | 752 | 2.62 | 0.95 | 9.00 | 9.83 | 445 | 42 | 450 | 46 | 447 | 3 |
| 43 (c) | 2.34 | bdl | 3986 | 759 | 588 | 2.59 | 0.97 | 8.91 | 12.41 | 465 | 43 | 363 | 46 | 414 | 72 |
| 44 (c) | 2.25 | bdl | 4074 | 785 | 490 | 2.52 | 0.98 | 8.59 | 14.64 | 488 | 44 | 308 | 46 | 398 | 128 |
| 45 (c) | 2.37 | bdl | 3821 | 685 | 739 | 2.67 | 0.97 | 9.77 | 10.02 | 424 | 43 | 456 | 47 | 440 | 23 |
| 46 (c) | 2.42 | bdl | 3956 | 707 | 755 | 2.59 | 0.95 | 9.54 | 9.76 | 426 | 42 | 454 | 46 | 440 | 20 |
| 47 (c) | 2.58 | bdl | 4253 | 766 | 649 | 2.43 | 0.93 | 8.79 | 11.31 | 431 | 40 | 367 | 43 | 399 | 46 |
| 48 (c) | 2.50 | bdl | 3977 | 694 | 726 | 2.57 | 0.95 | 9.64 | 10.22 | 409 | 41 | 428 | 45 | 419 | 13 |
| 49 (c) | 2.28 | bdl | 3863 | 723 | 723 | 2.65 | 0.98 | 9.28 | 10.29 | 456 | 44 | 456 | 49 | 456 | 0 |
| 50 (c) | 2.45 | bdl | 3932 | 734 | 588 | 2.60 | 0.95 | 9.19 | 12.49 | 440 | 42 | 354 | 45 | 397 | 61 |

standard deviations for correction factor are at ±1σ; number of analyses averaged to produce correction factor listed in parentheses

concentrations listed in ppm, except for Th (wt. %); bdl = below detection limits
c: core analysis, r: rim analysis

average core age: 418 Ma±41 Ma (1 s.d) (±5 1 s.e.), n = 62

averge rim age: 419 Ma±25 Ma (1 s.d) (±4 1 s.e.), n = 38

**Table 11**. Isotopic analysis information, monazite, sample T22

| pt # | c/r | 208Pb/ 232Th age(Ma) | 1 s.e. | 207Pb/ 235U age(Ma) | 1 s.e | 206Pb/ 238U age(Ma) | 1 s.e | 207Pb/ 206U age(Ma) | 1 s.e. | % rad 206Pb | % rad 207Pb | % rad 208Pb |
|---|---|---|---|---|---|---|---|---|---|---|---|---|
| a1 | c | 431 | 4 | 478 | 5 | 466 | 19 | 407 | 105 | 97.2 | 66.5 | 96.7 |
| a1@1 | c | 428 | 4 | 466 | 4 | 459 | 8 | **424** | 40 | 97.9 | 73.0 | 97.6 |
| a4 | c | 391 | 4 | 438 | 6 | 438 | 7 | **440** | 26 | 99.2 | 87.3 | 98.9 |
| a5 | c | 431 | 4 | 469 | 5 | 461 | 9 | **421** | 45 | 98.2 | 76.3 | 98.1 |
| a9 | c | 433 | 4 | 484 | 5 | 476 | 8 | **437** | 35 | 98.8 | 83.0 | 98.5 |
| a13 | c | 428 | 4 | 488 | 6 | 474 | 10 | **406** | 46 | 98.7 | 81.1 | 98.4 |
| a14 | c | 423 | 4 | 478 | 6 | 464 | 9 | **397** | 44 | 97.8 | 72.3 | 97.7 |
| b1 | c | | | | | | | **408** | 22 | | 88.2 | |
| b2 | c | | | | | | | **436** | 21 | | 88.7 | |
| b2@1 | c | | | | | | | **447** | 11 | | 88.7 | |
| b3 | c | | | | | | | **424** | 9 | | 89.4 | |
| b4 | c | | | | | | | **421** | 7 | | 89.8 | |
| b6 | c | | | | | | | **423** | 7 | | 91.0 | |
| b8 | c | | | | | | | **425** | 7 | | 88.9 | |
| b15 | c | | | | | | | **424** | 6 | | 89.6 | |
| b11 | c | | | | | | | **415** | 24 | | 88.9 | |
| a2 | r | 499 | 4 | 402 | 4 | 399 | | **383** | 64 | 98.4 | 77.4 | 98.8 |
| a3 | r | 482 | 4 | 457 | 4 | 448 | | **400** | 17 | 99.3 | 88.5 | 98.8 |
| a6 | r | 458 | 4 | 408 | 4 | 406 | | **395** | 55 | 98.3 | 77.1 | 98.0 |
| a7 | r | 337 | 3 | 513 | 5 | 498 | | 426 | 10 | 100.0 | 99.3 | 99.2 |
| a8 | r | 439 | 5 | 375 | 6 | 382 | | **423** | 38 | 99.0 | 85.0 | 99.4 |
| a10 | r | 405 | 3 | 388 | 5 | 376 | | 306 | 42 | 99.0 | 85.0 | 99.3 |
| a11 | r | 459 | 4 | 415 | 4 | 414 | | 411 | 17 | 99.3 | 89.4 | 99.3 |
| a12 | r | 491 | 4 | 434 | 4 | 429 | | **404** | 38 | 99.0 | 85.5 | 99.2 |
| b5 | r | | | | | | | **392** | 22 | | 89.6 | |
| b7 | r | | | | | | | **386** | 8 | | 90.3 | |
| b9 | r | | | | | | | **357** | 11 | | 89.1 | |
| b10 | c/r | | | | | | | 413 | 17 | | 91.5 | |
| b16 | r | | | | | | | **392** | 4 | | 89.6 | |

analyses with prefix “a” analyzed at UCLA, August 2000
analyses with prefix “b” analyzed at UCLA, August 2001

for information on Th $O_2$/Th and U O/U yields, see Spear et al. (submitted)

**bold** indicates $^{207}Pb/^{206}Pb$ age used in calculation of domain age (Spear et al., submitted)

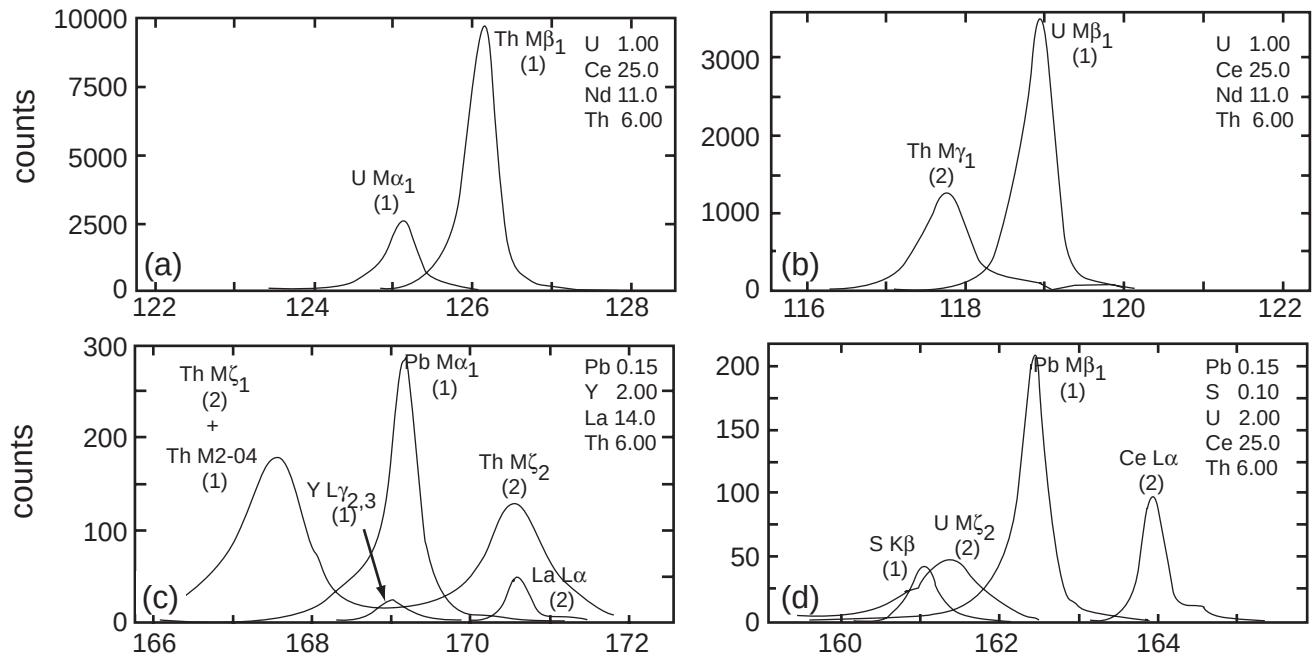
counts
(a)
U Mα1 (1)
Th Mβ1 (1)
U 1.00
Ce 25.0
Nd 11.0
Th 6.00
(b)
Th Mγ1 (2)
U Mβ1 (1)
U 1.00
Ce 25.0
Nd 11.0
Th 6.00
counts
(c)
Th Mζ1 (2) + Th M2-04 (1)
Y Lγ2,3 (1)
Pb Mα1 (1)
Th Mζ2 (2)
La Lα (2)
Pb 0.15
Y 2.00
La 14.0
Th 6.00
(d)
S Kβ (1)
U Mζ2 (2)
Pb Mβ1 (1)
Ce Lα (2)
Pb 0.15
S 0.10
U 2.00
Ce 25.0
Th 6.00

Figure 01

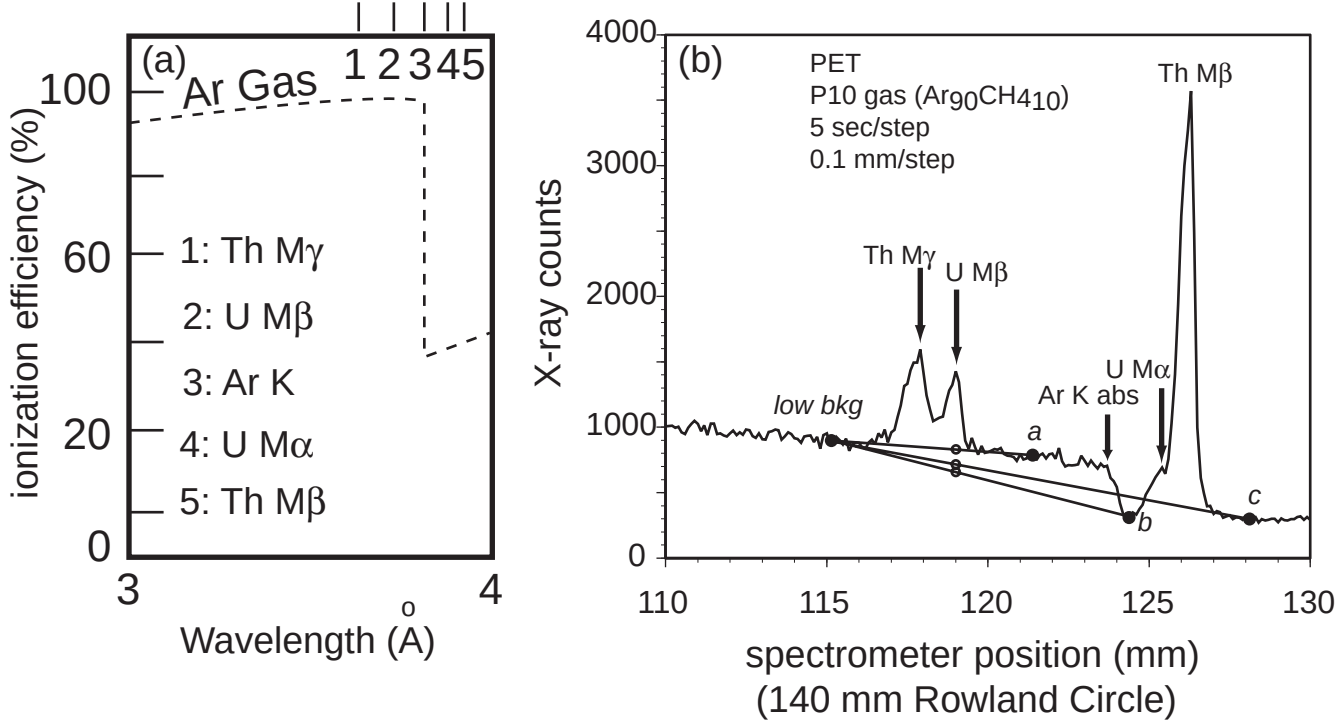
(a)
Ar Gas
1 2 3 4 5
100
60
20
0
ionization efficiency (%)
1: Th Mγ
2: U Mβ
3: Ar K
4: U Mα
5: Th Mβ
3
4
Wavelength (A)
o
(b)
PET
P10 gas (Ar90CH410)
5 sec/step
0.1 mm/step
Th Mβ
Th Mγ
U Mβ
U Mα
Ar K abs
low bkg
a
b
c
4000
3000
2000
1000
0
X-ray counts
110
115
120
125
130
spectrometer position (mm)
(140 mm Rowland Circle)

Figure 02

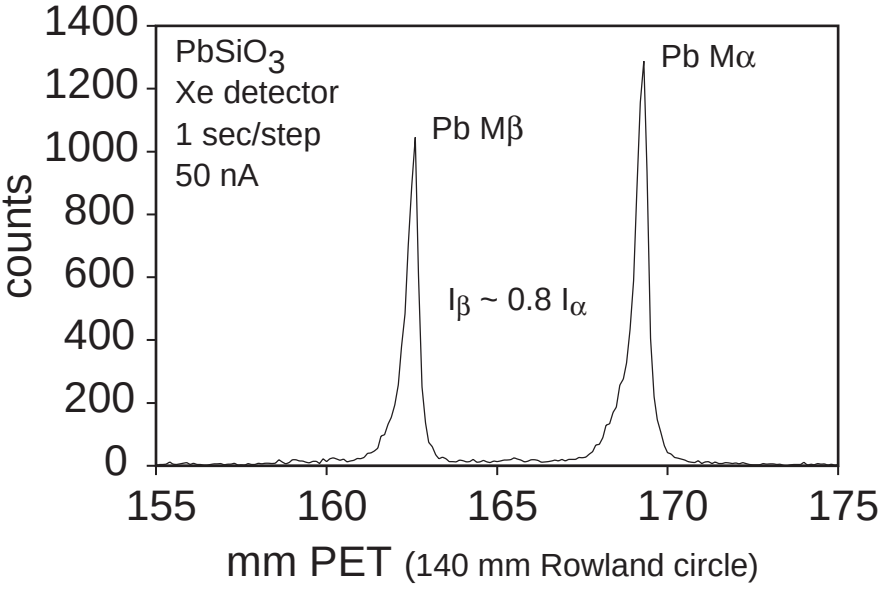
1400
1200
1000
800
600
400
200
0
counts
PbSiO3
Xe detector
1 sec/step
50 nA
Pb Mβ
Pb Mα
Iβ ~ 0.8 Iα
155
160
165
170
175
mm PET (140 mm Rowland circle)

Figure 03

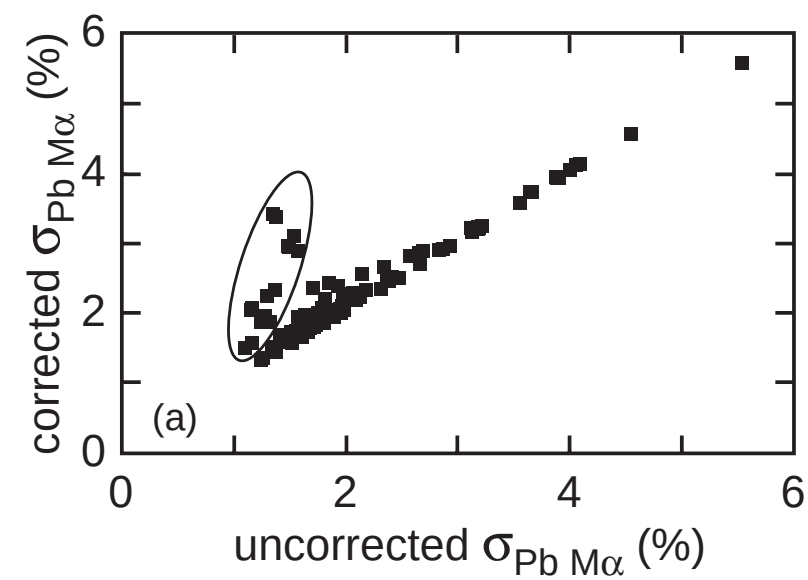
corrected σPb Mα (%)
uncorrected σPb Mα (%)
(a)
0
2
4
6

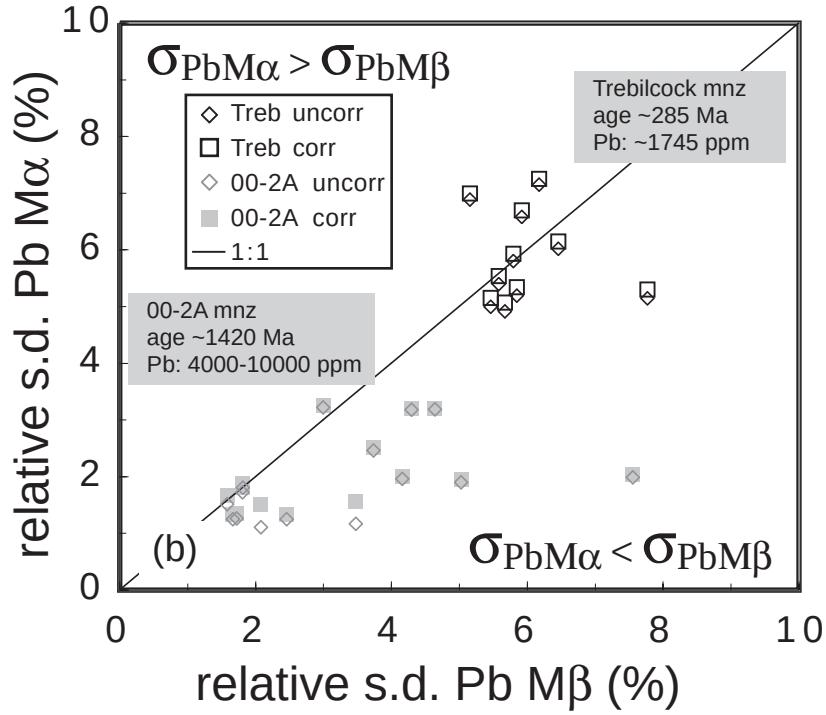
relative s.d. Pb Mα (%)
relative s.d. Pb Mβ (%)
σPbMα > σPbMβ
σPbMα < σPbMβ
Treb uncorr
Treb corr
00-2A uncorr
00-2A corr
1:1
Trebilcock mnz
age ~285 Ma
Pb: ~1745 ppm
00-2A mnz
age ~1420 Ma
Pb: 4000-10000 ppm
(b)
0
2
4
6
8
10

Figure 04

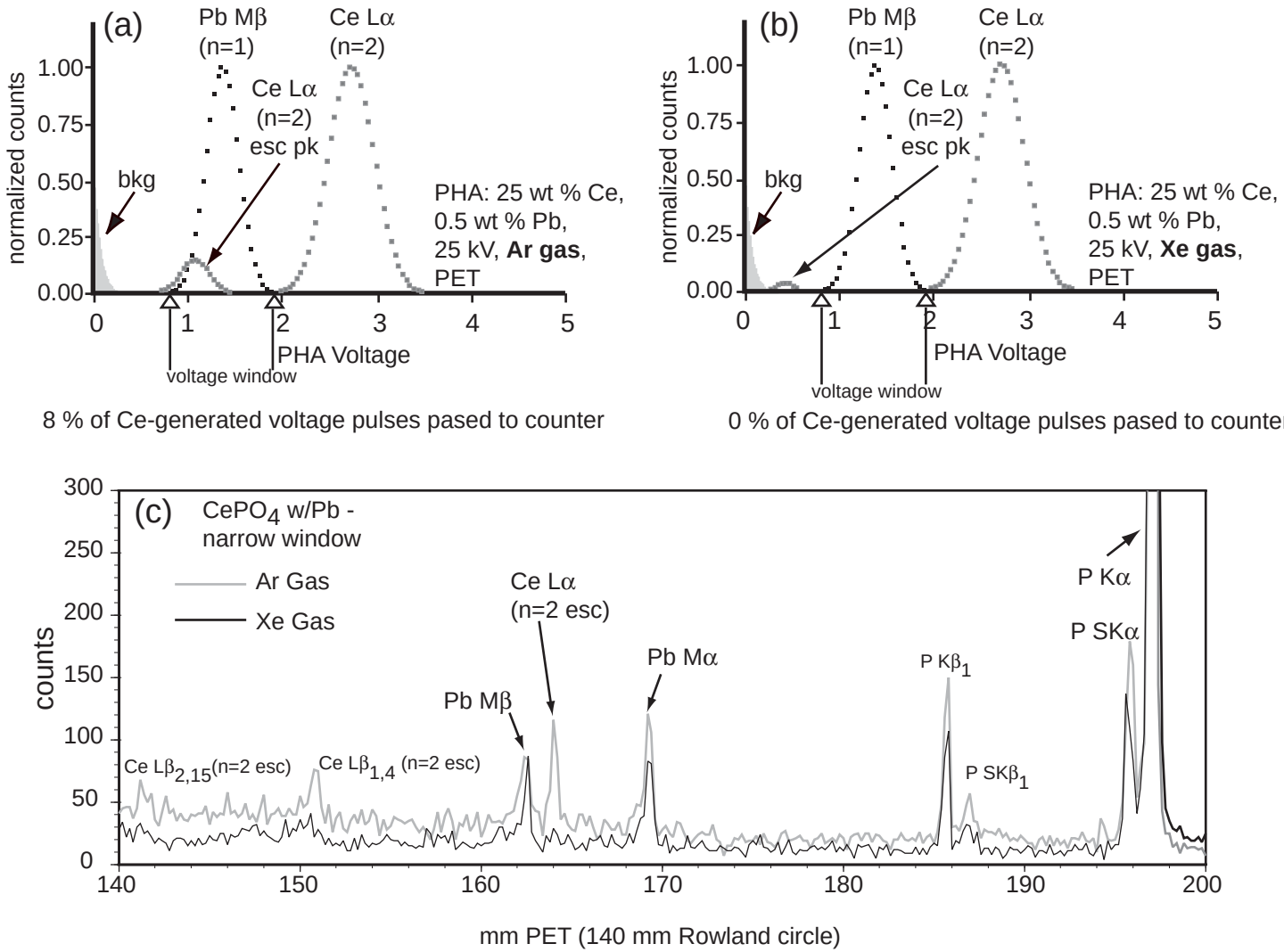


8 % of Ce-generated voltage pulses pased to counter

0 % of Ce-generated voltage pulses pased to counter

Figure 05

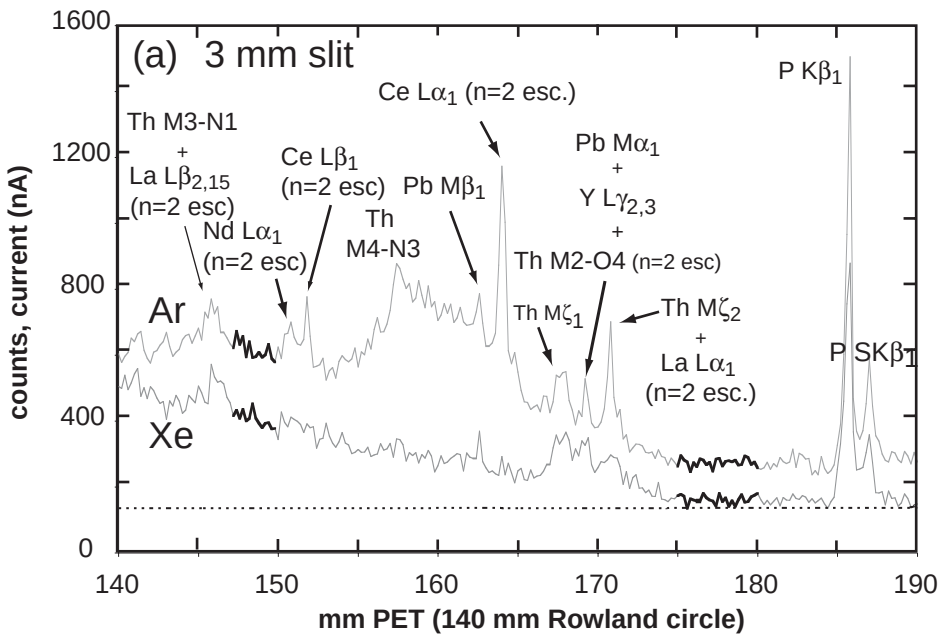
(a) 3 mm slit
Th M3-N1
+
La Lβ2,15
(n=2 esc)
Nd Lα1
(n=2 esc)
Ce Lβ1
(n=2 esc)
Th
M4-N3
Pb Mβ1
Ce Lα1 (n=2 esc.)
Th Mζ1
Pb Mα1
+
Y Lγ2,3
+
Th M2-O4 (n=2 esc)
Th Mζ2
+
La Lα1
(n=2 esc.)
P Kβ1
P SKβ1
Ar
Xe
counts, current (nA)
mm PET (140 mm Rowland circle)

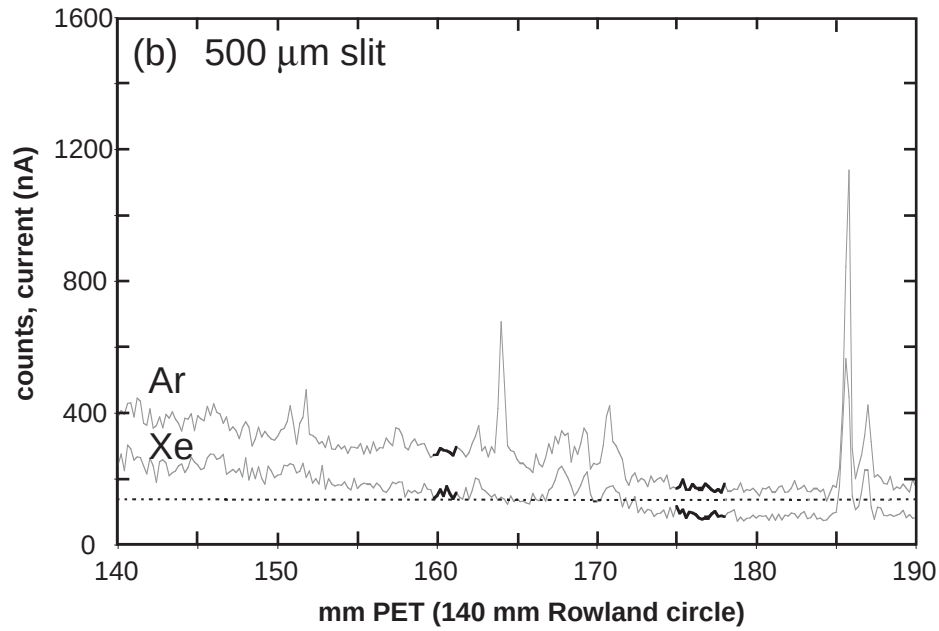
(b) 500 μm slit
Ar
Xe
counts, current (nA)
mm PET (140 mm Rowland circle)

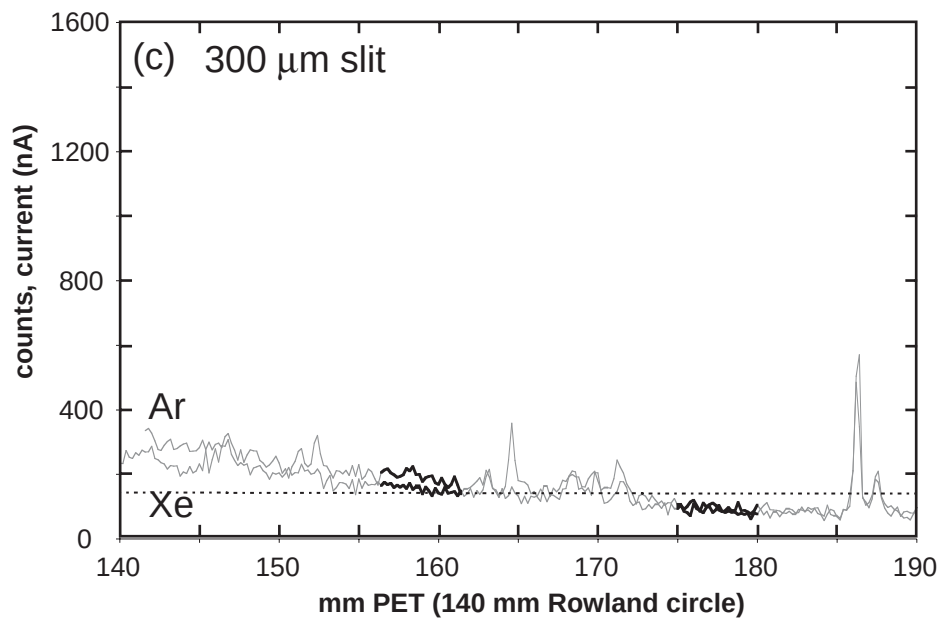
(c) 300 μm slit
Ar
Xe
counts, current (nA)
mm PET (140 mm Rowland circle)

Figure 06

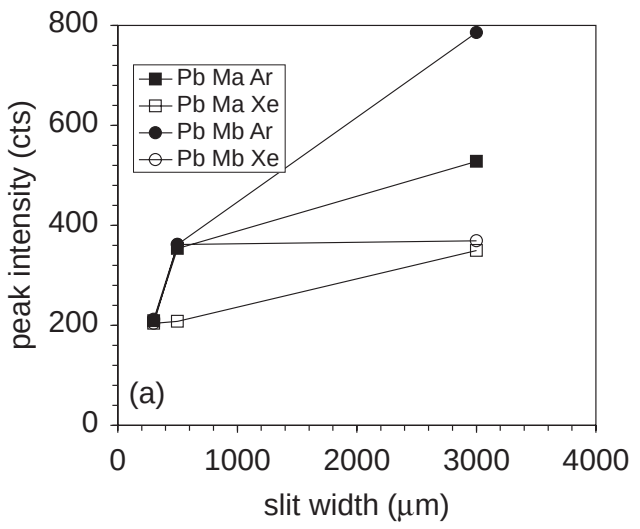
peak intensity (cts)
800
600
400
200
0
Pb Ma Ar
Pb Ma Xe
Pb Mb Ar
Pb Mb Xe
(a)
0
1000
2000
3000
4000
slit width (μm)

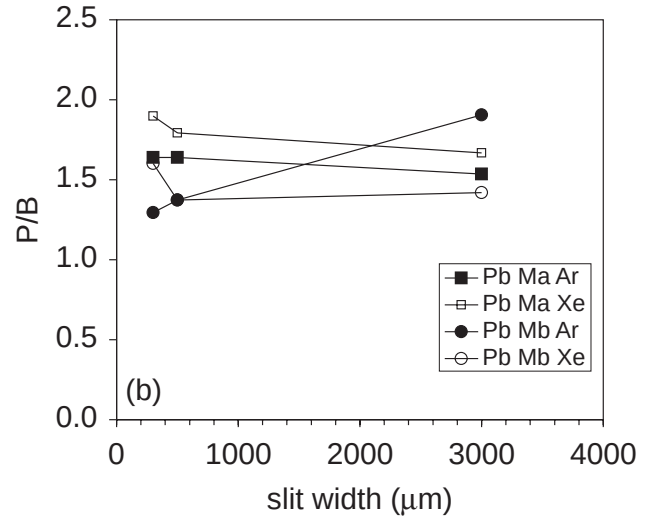
P/B
2.5
2.0
1.5
1.0
0.5
0.0
Pb Ma Ar
Pb Ma Xe
Pb Mb Ar
Pb Mb Xe
(b)
0
1000
2000
3000
4000
slit width (μm)

Figure 07

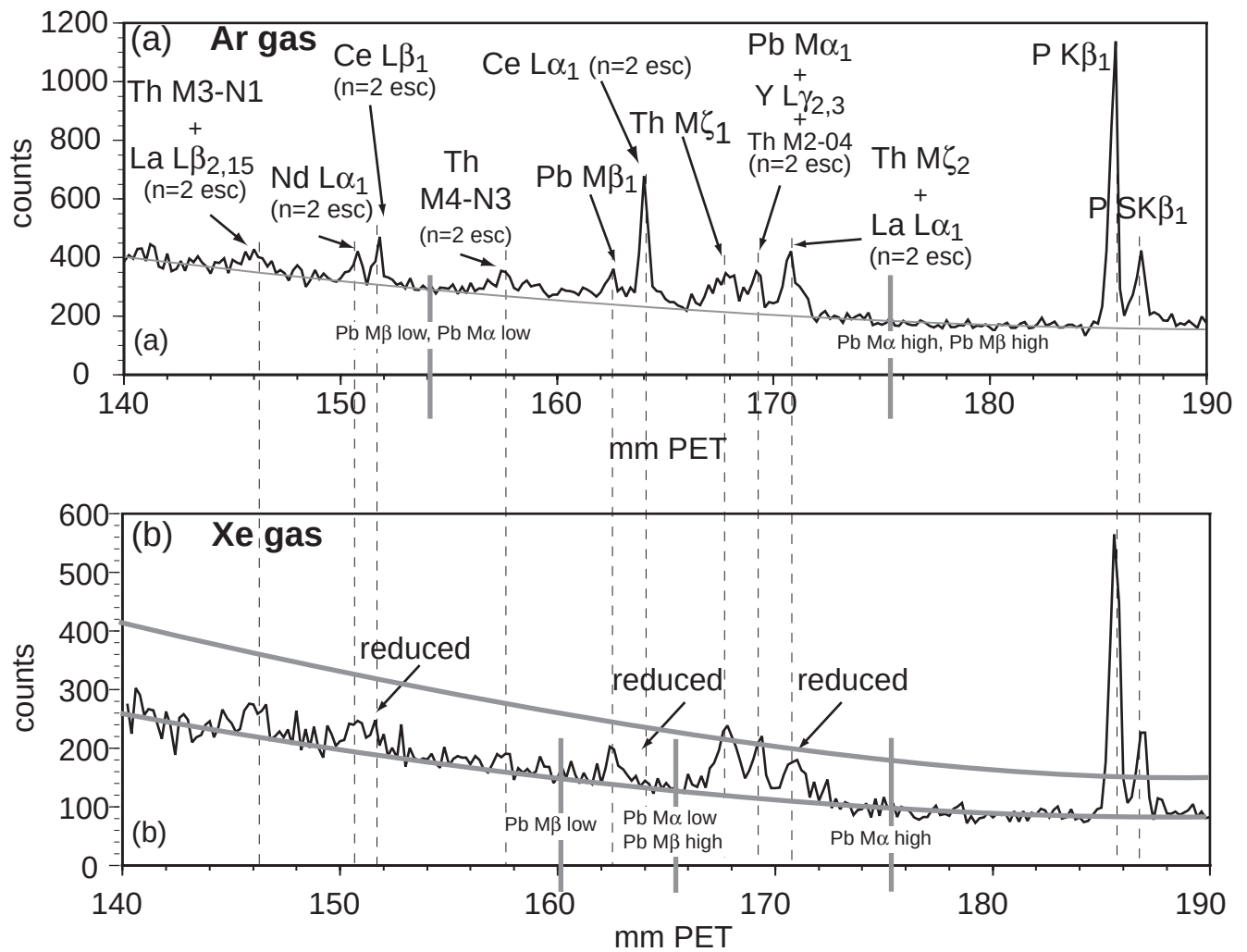
(a) Ar gas
Th M3-N1
+
La Lβ2,15
(n=2 esc)
Nd Lα1
(n=2 esc)
Ce Lβ1
(n=2 esc)
Th
M4-N3
(n=2 esc)
Ce Lα1 (n=2 esc)
Pb Mβ1
Th Mζ1
Pb Mα1
+
Y Lγ2,3
+
Th M2-04
(n=2 esc)
Th Mζ2
+
La Lα1
(n=2 esc)
P Kβ1
P SKβ1
Pb Mβ low, Pb Mα low
Pb Mα high, Pb Mβ high
counts
mm PET
(b) Xe gas
reduced
reduced
reduced
Pb Mβ low
Pb Mα low
Pb Mβ high
Pb Mα high

Figure 08

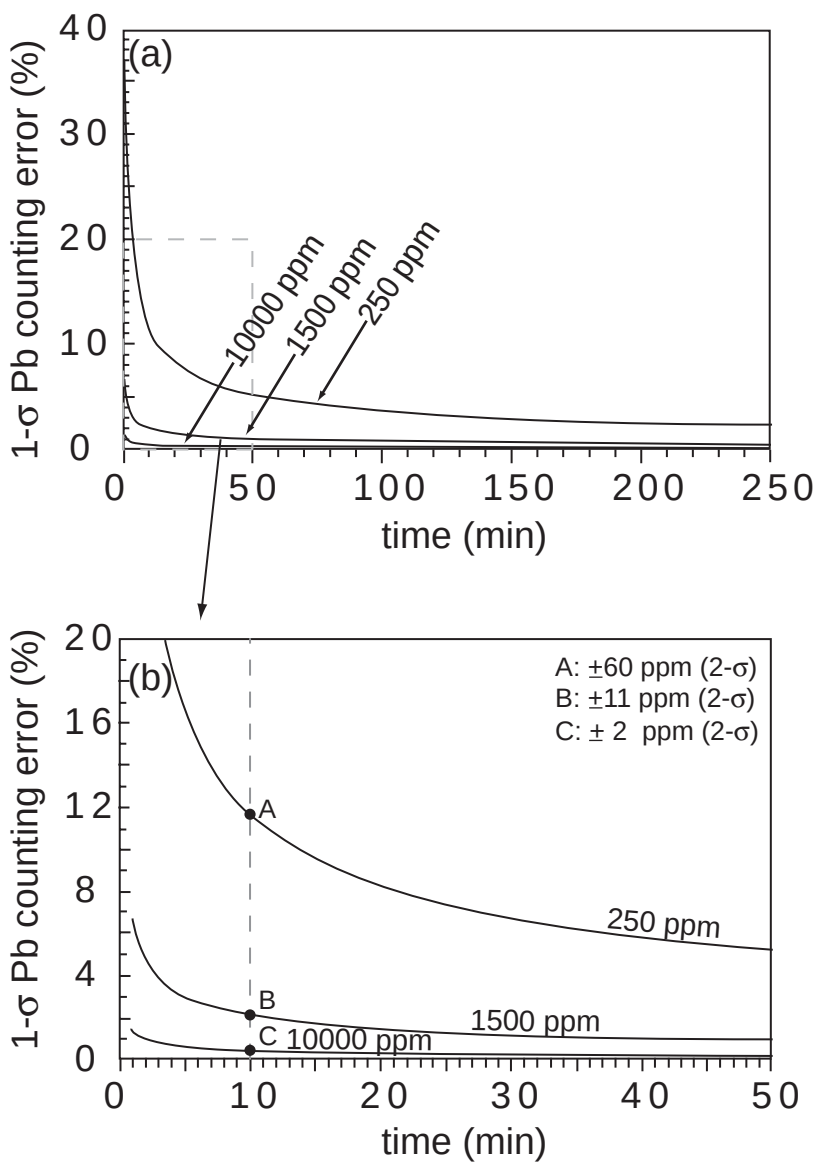
(a)
1-σ Pb counting error (%)
40
30
20
10
0
0
50
100
150
200
250
time (min)
10000 ppm
1500 ppm
250 ppm
(b)
1-σ Pb counting error (%)
20
16
12
8
4
0
0
10
20
30
40
50
time (min)
A: ±60 ppm (2-σ)
B: ±11 ppm (2-σ)
C: ± 2 ppm (2-σ)
A
B
C
250 ppm
1500 ppm
10000 ppm

Figure 09

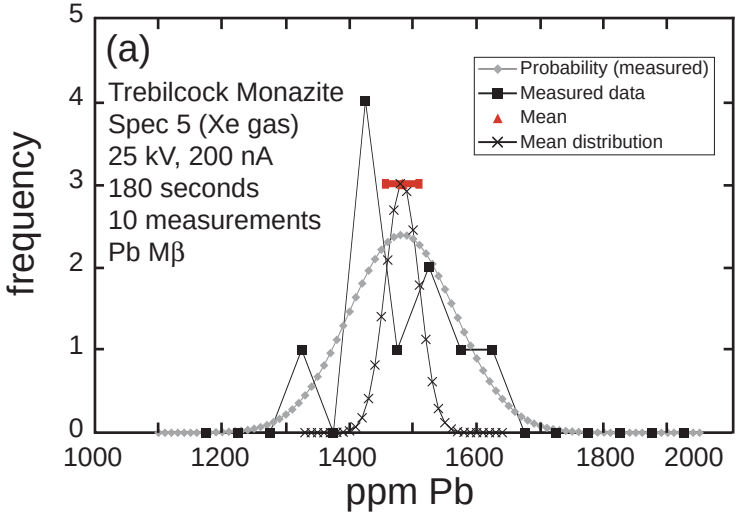
(a)
Trebilcock Monazite
Spec 5 (Xe gas)
25 kV, 200 nA
180 seconds
10 measurements
Pb Mβ
Probability (measured)
Measured data
Mean
Mean distribution
frequency
ppm Pb
0
1
2
3
4
5
1000
1200
1400
1600
1800
2000

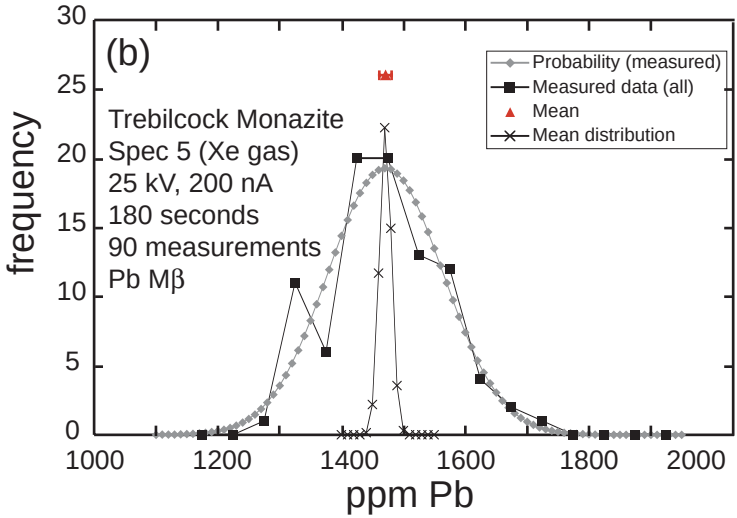
(b)
Trebilcock Monazite
Spec 5 (Xe gas)
25 kV, 200 nA
180 seconds
90 measurements
Pb Mβ
Probability (measured)
Measured data (all)
Mean
Mean distribution
frequency
ppm Pb
0
5
10
15
20
25
30
1000
1200
1400
1600
1800
2000

Figure 10

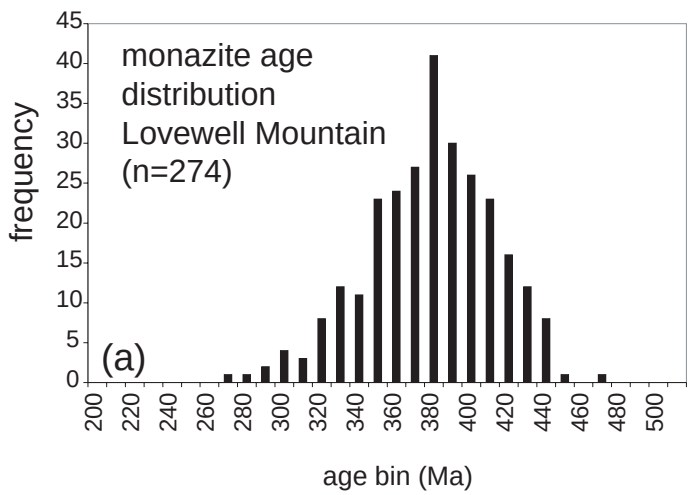
monazite age
distribution
Lovewell Mountain
(n=274)
(a)
frequency
age bin (Ma)

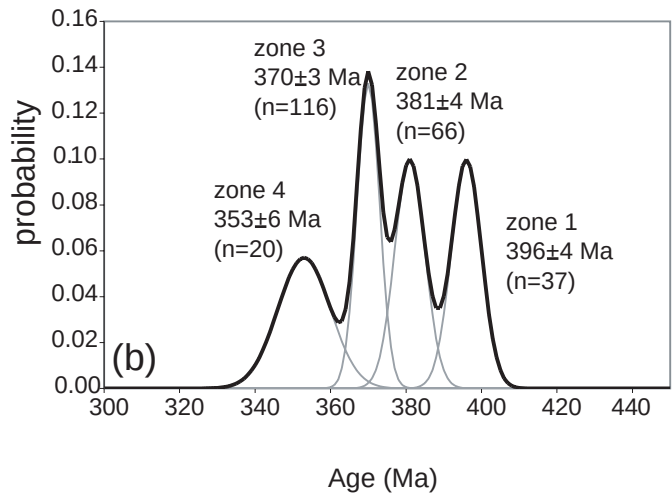
zone 3
370±3 Ma
(n=116)
zone 2
381±4 Ma
(n=66)
zone 4
353±6 Ma
(n=20)
zone 1
396±4 Ma
(n=37)
(b)
probability
Age (Ma)

Figure 11

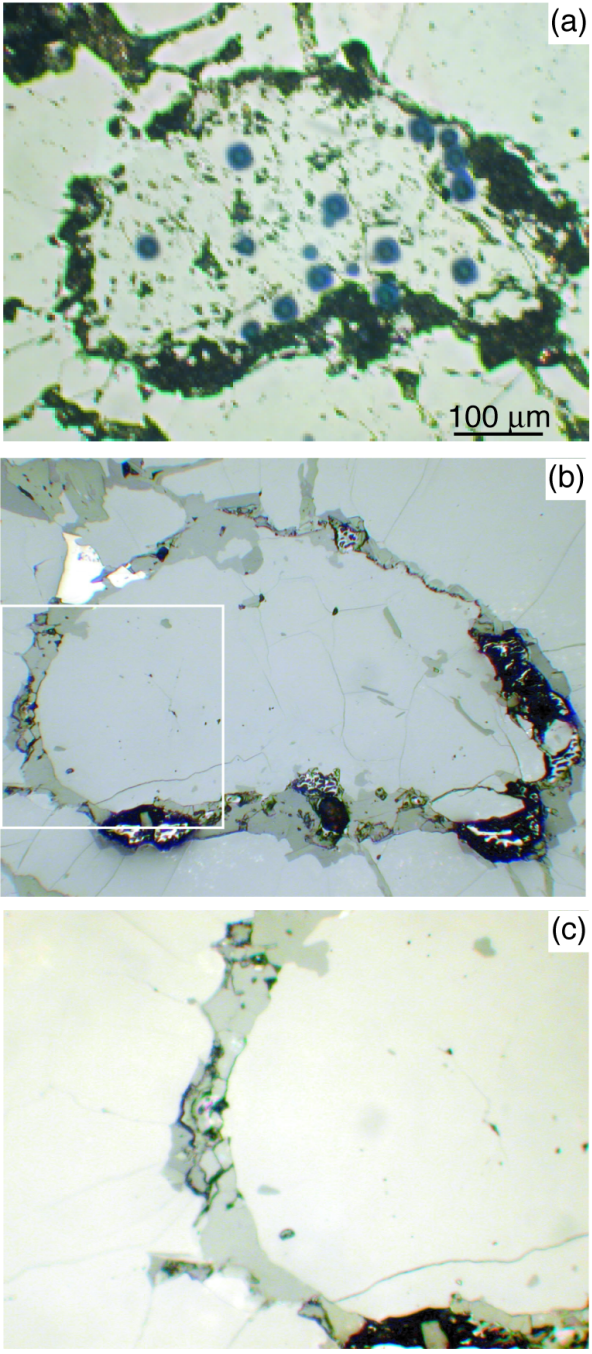


Figure 12

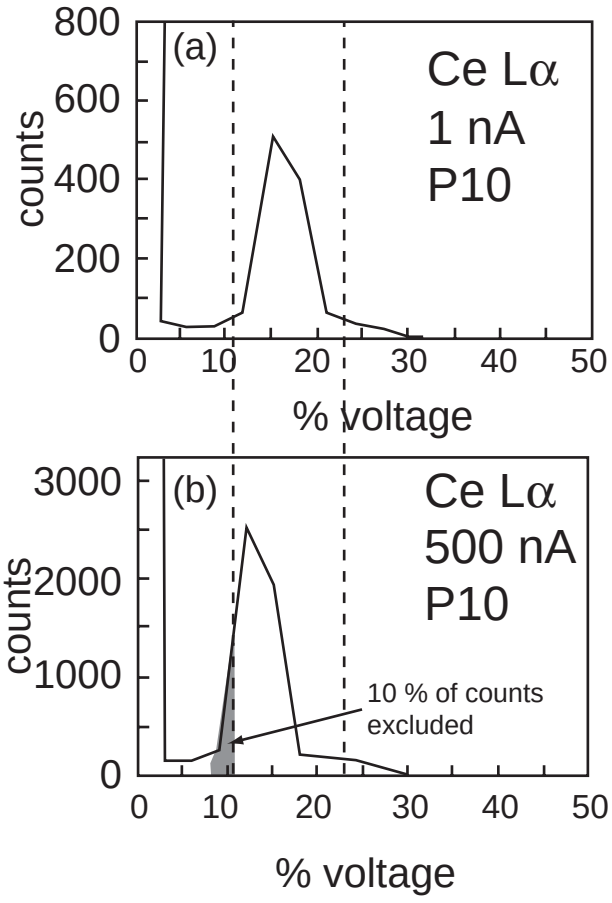
(a)
Ce Lα
1 nA
P10
counts
800
600
400
200
0
0
10
20
30
40
50
% voltage
(b)
Ce Lα
500 nA
P10
counts
3000
2000
1000
0
10 % of counts
excluded
0
10
20
30
40
50
% voltage

Figure 13

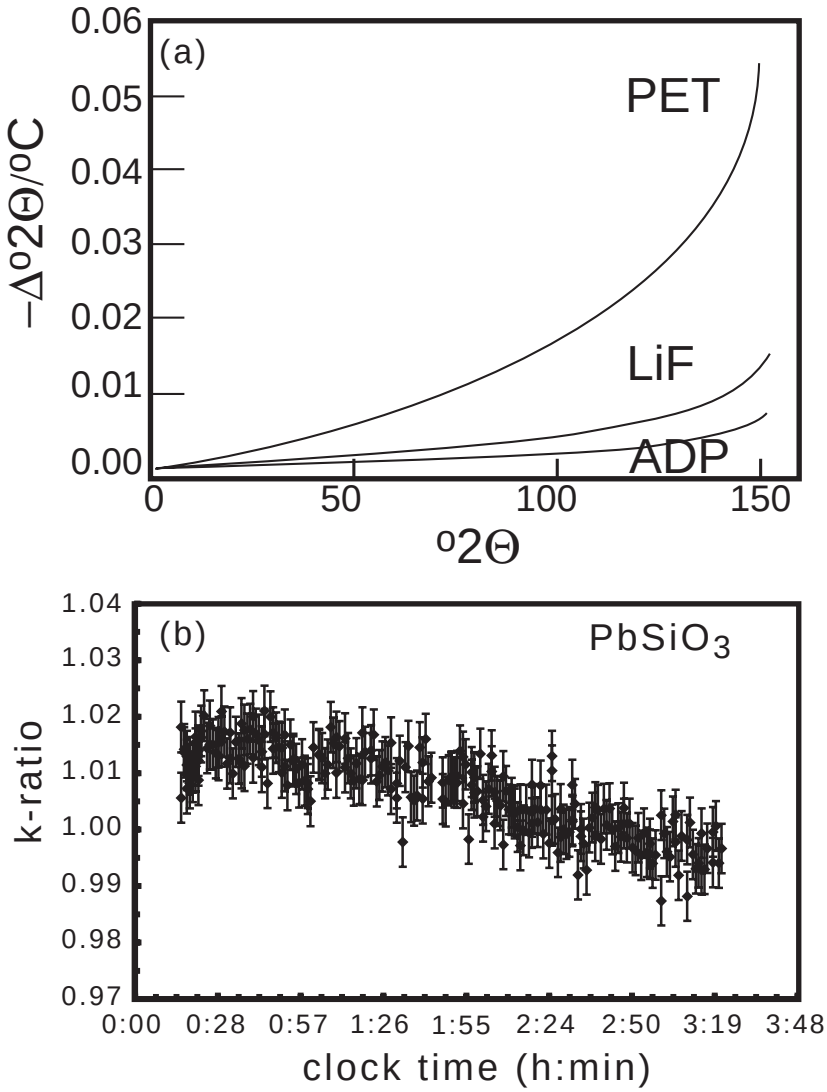
(a)
PET
LiF
ADP
0.06
0.05
0.04
0.03
0.02
0.01
0.00
0
50
100
150
−Δ°2Θ/°C
°2Θ
(b)
PbSiO3
1.04
1.03
1.02
1.01
1.00
0.99
0.98
0.97
k-ratio
0:00
0:28
0:57
1:26
1:55
2:24
2:50
3:19
3:48
clock time (h:min)

Figure 14

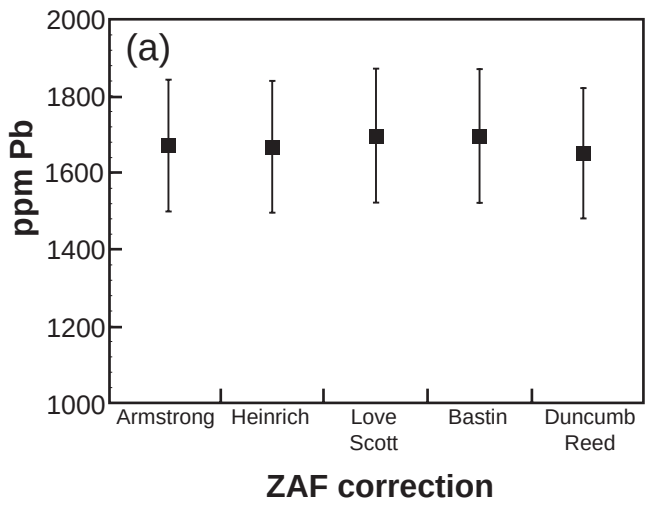
(a)
ppm Pb
2000
1800
1600
1400
1200
1000
Armstrong
Heinrich
Love
Scott
Bastin
Duncumb
Reed
ZAF correction

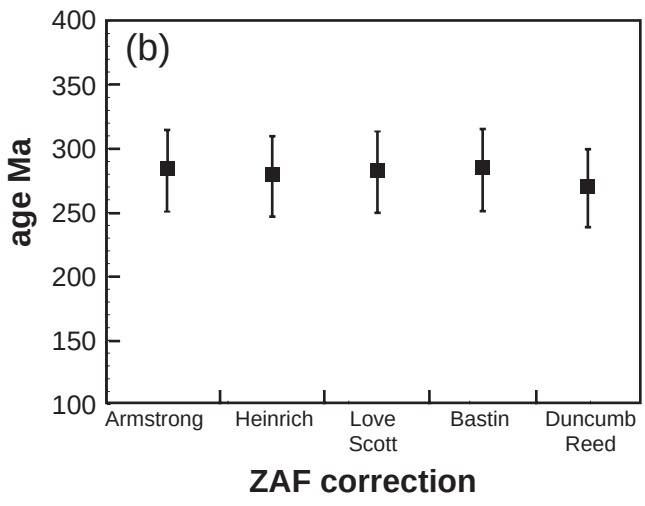
(b)
age Ma
400
350
300
250
200
150
100
Armstrong
Heinrich
Love
Scott
Bastin
Duncumb
Reed
ZAF correction

Figure 15

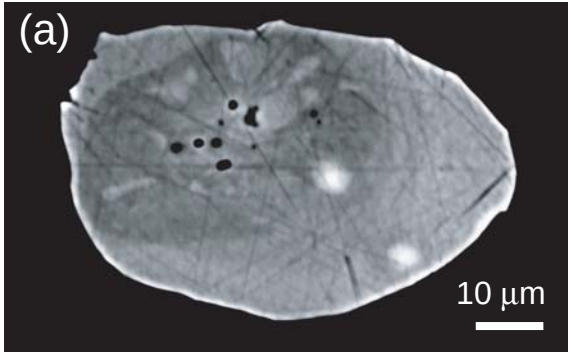
(a)
10 μm

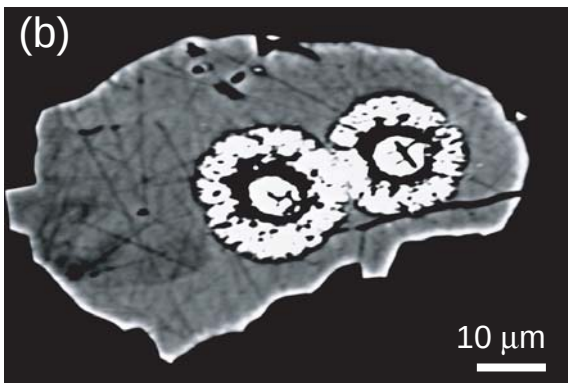
(b)
10 μm

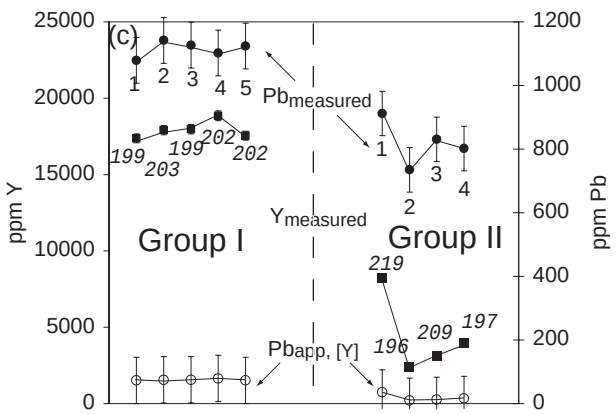
(c)
25000
20000
15000
10000
5000
0
ppm Y
1200
1000
800
600
400
200
0
ppm Pb
1
2
3
4
5
Pbmeasured
199
203
199
202
202
1
2
3
4
Ymeasured
Group I
Group II
219
196
209
197
Pbapp, [Y]

Figure 16

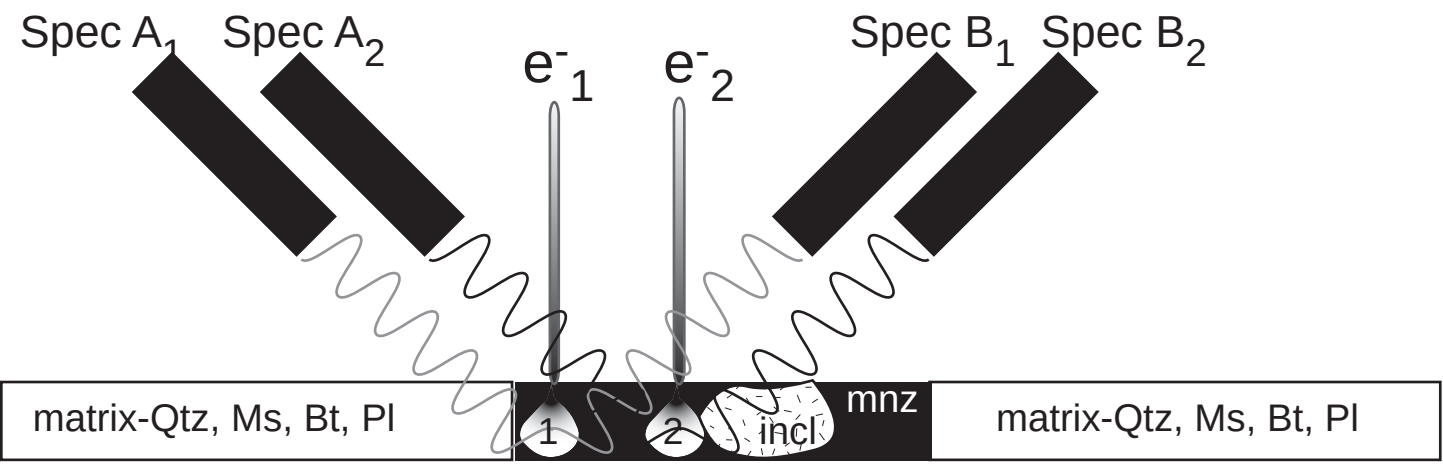
Spec A1
Spec A2
e-1
e-2
Spec B1
Spec B2
matrix-Qtz, Ms, Bt, Pl
1
2
incl
mnz
matrix-Qtz, Ms, Bt, Pl

Figure 17

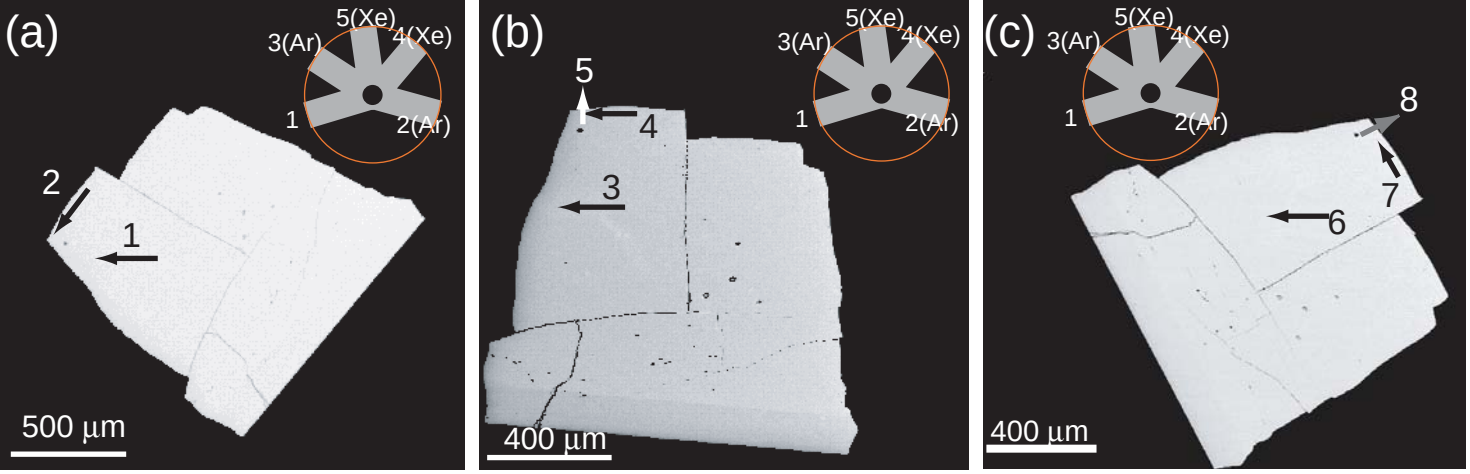
(a)
5(Xe)
3(Ar)
4(Xe)
1
2(Ar)
2
1
500 µm
(b)
5(Xe)
3(Ar)
4(Xe)
1
2(Ar)
5
4
3
400 µm
(c)
5(Xe)
3(Ar)
4(Xe)
1
2(Ar)
8
7
6
400 µm

Figure 18

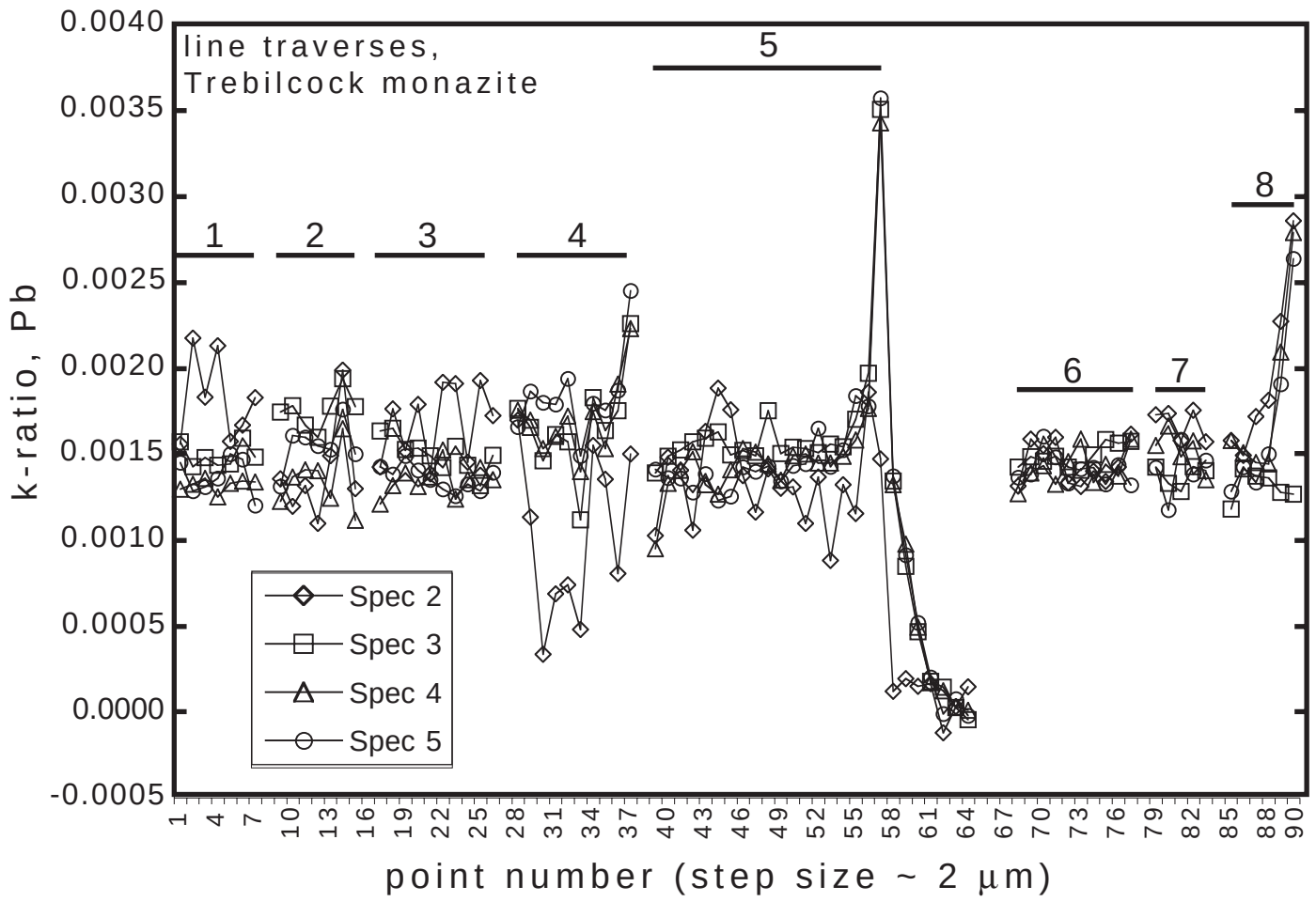
line traverses,
Trebilcock monazite
1
2
3
4
5
6
7
8
Spec 2
Spec 3
Spec 4
Spec 5
k-ratio, Pb
0.0040
0.0035
0.0030
0.0025
0.0020
0.0015
0.0010
0.0005
0.0000
-0.0005
1 4 7 10 13 16 19 22 25 28 31 34 37 40 43 46 49 52 55 58 61 64 67 70 73 76 79 82 85 88 90
point number (step size ~ 2 μm)

Figure 19

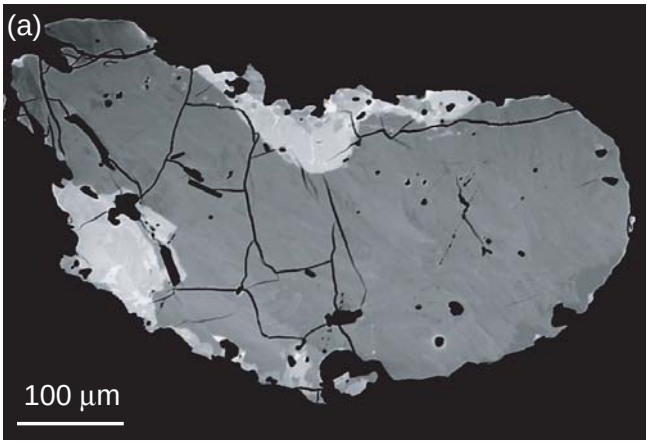


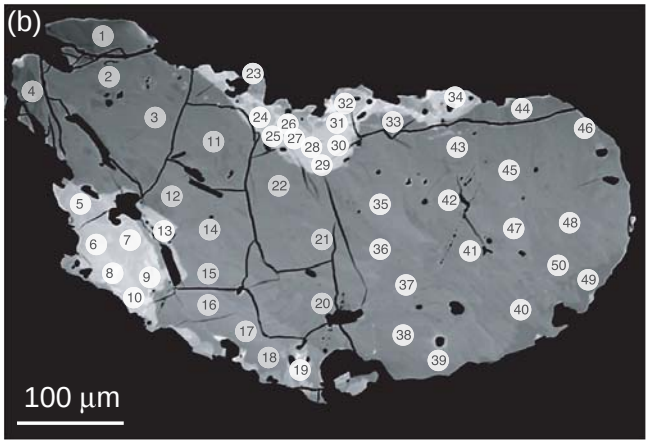


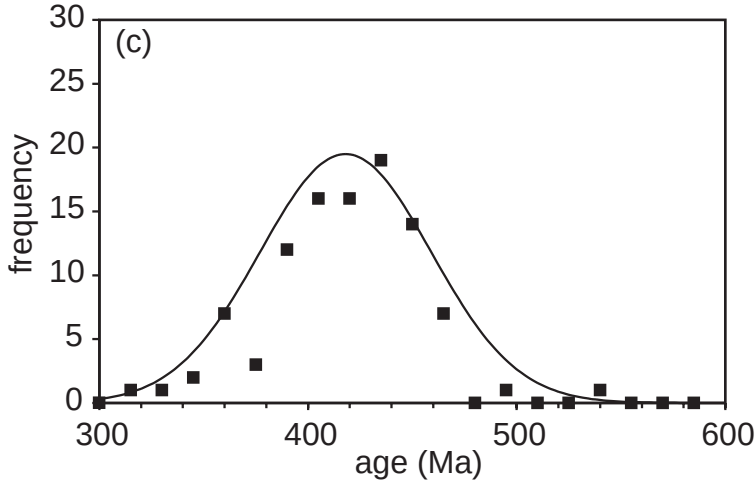


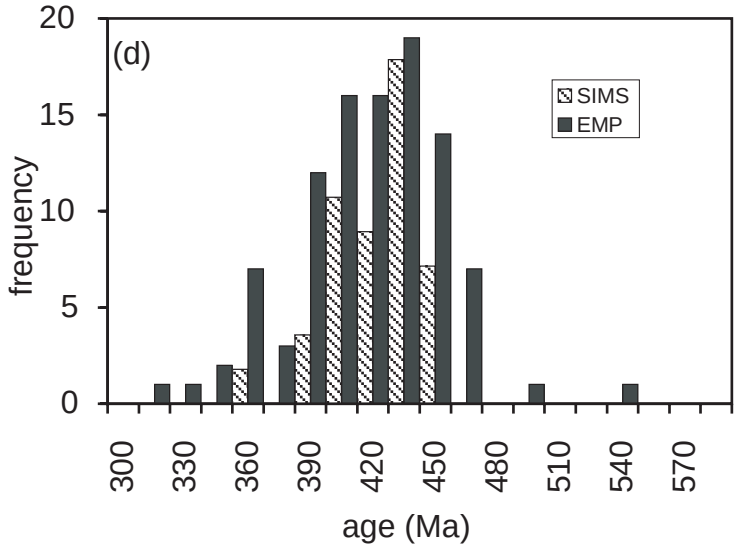


Figure 20

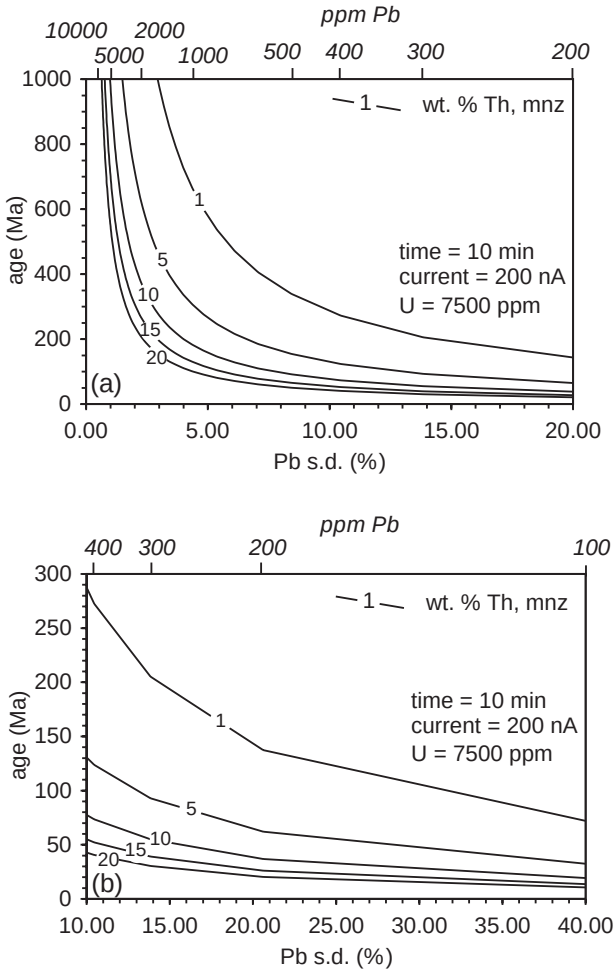
ppm Pb
10000
2000
5000
1000
500
400
300
200
1000
800
600
400
200
0
age (Ma)
1
wt. % Th, mnz
1
5
10
15
20
time = 10 min
current = 200 nA
U = 7500 ppm
(a)
0.00
5.00
10.00
15.00
20.00
Pb s.d. (%)
ppm Pb
400
300
200
100
300
250
200
150
100
50
0
age (Ma)
1
wt. % Th, mnz
time = 10 min
current = 200 nA
U = 7500 ppm
1
5
10
15
20
(b)
10.00
15.00
20.00
25.00
30.00
35.00
40.00
Pb s.d. (%)

Figure 21

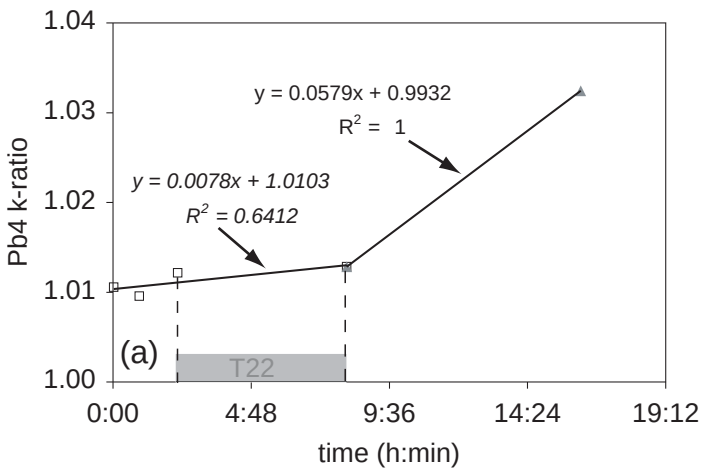
1.04
1.03
1.02
1.01
1.00
Pb4 k-ratio
y = 0.0579x + 0.9932
R2 = 1
y = 0.0078x + 1.0103
R2 = 0.6412
(a)
T22
0:00
4:48
9:36
14:24
19:12
time (h:min)

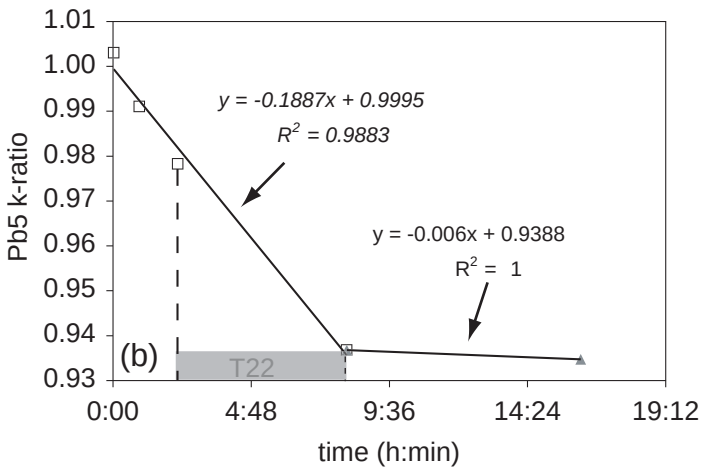
1.01
1.00
0.99
0.98
0.97
0.96
0.95
0.94
0.93
Pb5 k-ratio
y = -0.1887x + 0.9995
R2 = 0.9883
y = -0.006x + 0.9388
R2 = 1
(b)
T22
0:00
4:48
9:36
14:24
19:12
time (h:min)

Figure A1